ACS NANO

www.acsnano.org

Article

Biomimetic Nanozyme-Decoys Reprogram Immune Niches to Intercept Colitis-Carcinoma Transition

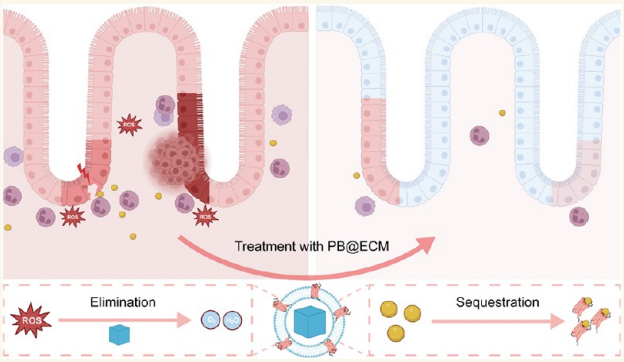
Qi Sun, Wanling Liu, Sijie Li, Xiwen Chen, Hanjie Zhang, Dongze Mo, Pinwen Zhou, Xiaomiao Cui, Di Huang, Bing Xia, Jingjing Zhang,* Xinying Wang,* Xiaoyu Wang,* and Hui Wei*

Cite This: https://doi.org/10.1021/acsnano.6c16014

Read Online

ACCESS | Metrics & More | Article Recommendations | Supporting Information

ABSTRACT: Colitis-associated colorectal cancer (CAC) arises from chronic inflammatory niches characterized by persistent oxidative stress and dysregulated immune cell recruitment. Current anti-inflammatory therapies provide only transient symptom relief and fail to prevent malignant progression due to their inability to simultaneously mitigate oxidative injury and immune chemotaxis. Our analysis of clinical samples revealed markedly elevated C-X-C motif chemokine ligand 2 (CXCL2) in intestinal tissues from patients with inflammatory bowel disease and CAC, implicating the CXCL2-CXCR2 (C-X-C motif chemokine receptor 2) axis in driving excessive neutrophil and macrophage infiltration and fostering tumorigenesis. Herein, we report a biomimetic nanozyme (PB@ECM) that reprograms inflammatory immune niches to intercept CAC progression. PB@ECM integrates a Prussian blue nanozyme core with genetically engineered macrophage membranes, enabling concurrent scavenging of reactive oxygen species through superoxide dismutase- and catalase-like activities and sequestration of CXCL2 via membrane-displayed CXCR2 receptors. In murine models of colitis and CAC, PB@ECM significantly alleviated intestinal inflammation, suppressed neutrophil and macrophage infiltration, and effectively inhibited colitis-carcinoma transition. Notably, treatment with PB@ECM significantly prolonged survival compared with other groups. By disrupting the pathological crosstalk between oxidative stress and immune chemotaxis, this work establishes a biomimetic nanozyme strategy for preventing inflammation-driven carcinogenesis.



KEYWORDS: *nanozymes, chronic inflammation, reactive oxygen species, immune niches, colitis-carcinoma transition*

INTRODUCTION

Chronic inflammation has long been recognized as a central driver of cancer initiation and progression.[1−6] Persistent inflammatory microenvironments sustain excessive production of reactive oxygen species (ROS) and proinflammatory mediators, leading to DNA damage, genomic instability, and oncogenic mutations.[6,7] Concurrently, prolonged infiltration of innate immune cells, particularly neutrophils and macrophages, further accelerates tumorigenesis through continuous secretion of cytokines such as interleukin-1β (IL-1β) and tumor necrosis factor-α (TNF-α), which activate oncogenic signaling pathways, promote epithelial proliferation, and suppress apoptosis. Despite this well-established causal link, effective strategies to intercept the transition from chronic inflammation to cancer remain scarce, largely because current therapeutic paradigms focus on symptomatic inflammation control while overlooking key immune cell-driven malignant transformation.[8,9]

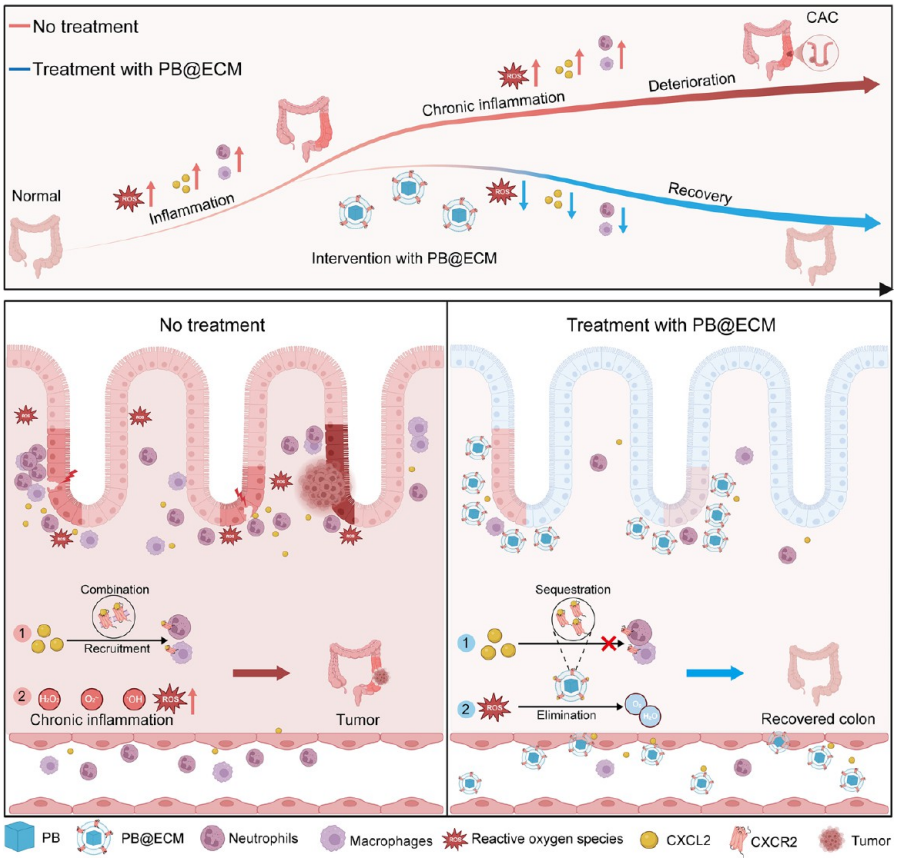
Colitis-associated colorectal cancer (CAC) represents a prototypical and clinically devastating model of inflammation-driven carcinogenesis.[10] Emerging from long-standing inflammatory bowel diseases (IBD),[11] including ulcerative colitis[12] and Crohn's disease,[13] CAC follows a chronic inflammation-dominated oncogenic trajectory that is distinct from sporadic colorectal cancer and is associated with poor prognosis.[14,15] Existing IBD therapies, such as nonsteroidal anti-inflammatory drugs and biologics, primarily suppress inflammatory symptoms and often provide only transient benefit. In patients with sustained disease activity, extensive immune cell infiltration, and repeated inflammatory insults, merely attenuating inflammation is insufficient to halt malignant transformation. These limitations underscore an unmet need for therapeutic strategies that go beyond inflammation relief and actively disrupt immune cell-driven mechanisms propelling chronic inflammation toward cancer.

Received: August 19, 2026
Revised: November 1, 2026
Accepted: November 3, 2026

ACS Publications © XXXX American Chemical Society

Downloaded from pubs.acs.org/ancac3/article-pdf/doi/10.1021/acsnano.6c16014/6914824O/acsnano.6c16014.pdf?guestAccessKey=8de0abfb-c7d9-4588-addc-2b5c448d3cea by NANJING UNIV user on 12 November 2026

Scheme 1. Schematic Illustration of PB@ECM Nanoformulation for Intercepting Transition from Chronic Colitis to Colorectal Cancer[a]



[a]Without proper treatment, chronic inflammation in IBD elevates ROS and releases chemokines that recruit immune cells, ultimately driving malignant progression to colorectal cancer. Treatment with the dual-function PB@ECM, the macrophage membrane coating with overexpressed CXCR2, enables precise targeting of colonic inflammation sites. The PB core scavenges ROS, while ECM, *via* CXCR2, sequesters CXCL2 and inhibits the CXCL2-CXCR2 axis-mediated recruitment of neutrophils and macrophages. Together, PB@ECM reduces ROS-mediated damage and suppresses recruitment-mediated proinflammatory responses, thereby alleviating the malignant transformation from chronic colitis to colorectal cancer.

Chemokine-mediated immune cell recruitment has emerged as a central contributor to inflammation-driven carcinogenesis.[16,17] Previous studies have established that CXCL2-CXCR2 signaling promotes neutrophil recruitment.[18,19] Here, we provide further evidence that the C-X-C motif chemokine ligand 2 (CXCL2)-CXCR2 (C-X-C motif chemokine receptor 2) axis is a key driver of immune cell recruitment during the IBD-to-CAC transition. CXCL2, abundantly secreted by inflamed intestinal tissues, promotes excessive infiltration of neutrophils and macrophages via CXCR2 engagement, establishing a feed-forward loop that sustains tissue injury and fosters a tumor-promoting immune niche. We therefore hypothesized that effective interception of colitis-to-cancer progression requires simultaneous suppression of inflammation-associated oxidative stress and blockade of CXCL2-CXCR2-driven immune cell recruitment.

Here, we report a genetically engineered biomimetic nanozyme that integrates these two functions into a single therapeutic platform (Scheme 1). By coating genetically engineered macrophage membranes (ECM) onto Prussian blue (PB) nanozymes, we developed PB@ECM to simultaneously scavenge inflammatory ROS and neutralize CXCL2. PB, an FDA-approved material for metal detoxification, exhibits intrinsic superoxide dismutase (SOD)-, catalase (CAT)-, and hydroxyl radical-scavenging activities, enabling efficient mitigation of oxidative stress in inflamed tissues.[20,21] Meanwhile, the ECM is engineered to overexpress CXCR2, allowing sequestration of CXCL2 and suppression of excessive neutrophil and macrophage infiltration. Conventional cell-membrane-coated nanozymes primarily rely on passive inflammation homing, immune evasion, or broad cytokine neutralization but lack specific chemokine-receptor blockade. Chemokine-receptor decoys can sequester chemokines but generally lack catalytic antioxidant capacity. Antioxidant nanomedicines reduce oxidative stress but do not directly block immune cell recruitment. In contrast, PB@ECM has dual action: ROS scavenging lowers inflammatory signaling, while reduced neutrophil/macrophage infiltration further decreases ROS production, thereby helping to break the ROS-immune cycle that drives colitis-carcinoma transition. Using murine models of colitis and CAC, we demonstrate that PB@ECM markedly attenuates inflammatory injury, reduces innate immune cell infiltration, prevents the development of CAC, and significantly prolongs survival (Scheme 1).

Together, this work establishes a biomimetic nanozyme strategy for reprogramming inflammatory immune niches to block inflammation-driven carcinogenesis.

https://doi.org/10.1021/acsnano.6c16014
ACS Nano XXXX, XXX, XXX−XXX

Downloaded from pubs.acs.org/ancac3/article-pdf/doi/10.1021/acsnano.6c16014/6914824O/acsnano.6c16014.pdf?guestAccessKey=8de0abfb-c7d9-4588-addc-2b5c448d3cea by NANJING UNIV user on 12 November 2026

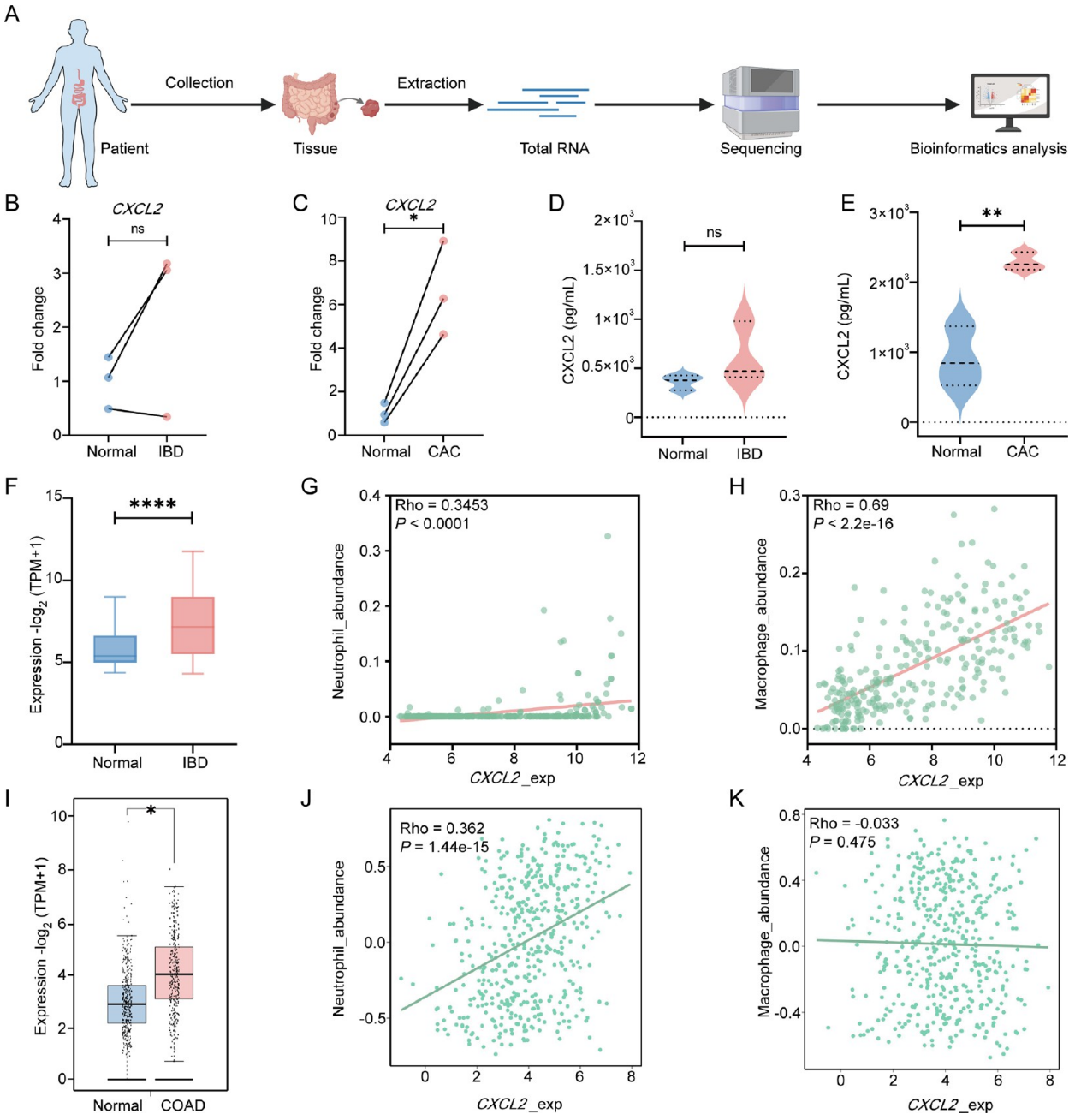


Figure 1. Correlation between CXCL2 expression and immune cell infiltration in patients. A, Flowchart of transcriptome sequencing for colonic tissues from patients. B, Gene expression of *CXCL2* in colon tissues from normal and IBD patients. C, Gene expression of *CXCL2* in colon tissues from normal and CAC patients. D, ELISA measurement of CXCL2 levels in colon tissues from normal and IBD patients ($n = 3$). E, ELISA measurement of CXCL2 levels in colon tissues from normal and CAC patients ($n = 3$). F, Gene expression of *CXCL2* in colon tissues from normal and IBD patients (normal, $n = 99$; IBD, $n = 265$). G, Correlation analysis examining correlation between *CXCL2* expression and neutrophil infiltration in IBD patients ($n = 265$). H, Correlation analysis examining relationships between macrophage and *CXCL2* in IBD patients ($n = 265$). I, Gene expression of *CXCL2* in colon tissues from normal ($n = 349$) and COAD ($n = 275$) patients. J, Correlation analysis examining correlation between *CXCL2* expression and neutrophil infiltration in COAD patients ($n = 459$). K, Correlation analysis examining relationships between macrophage and *CXCL2* in COAD patients ($n = 459$). ns, no significant difference, $*p < 0.05$, $**p < 0.01$, $****p < 0.0001$.

RESULTS/DISCUSSION

CXCL2 Overexpression and Immune Cell Infiltration in Clinical Samples

Alleviating oxidative stress alone is insufficient to prevent chronic inflammation from progressing to cancer. Instead, multiple therapeutic actions targeting pathological processes are required to halt this deterioration. To characterize the pathological environment at lesion sites in IBD and CAC, we performed transcriptome sequencing on colon tissues from patients with IBD, CAC, and healthy controls (Figure 1A, Tables S1 and S2). Principal component analysis revealed distinct transcriptomic profiles between the normal and diseased groups (Figures S1 and S2). Pro-inflammatory genes, including *IL-1β* and *IL-1α*, were markedly upregulated in both IBD and CAC tissues (Figures S1D and S2D). Notably, compared with healthy controls, *CXCL2* expression showed an upward trend in patients with IBD but was significantly increased in patients with

https://doi.org/10.1021/acsnano.6c16014
ACS Nano XXXX, XXX, XXX−XXX

Downloaded from pubs.acs.org/ancac3/article-pdf/doi/10.1021/acsnano.6c16014/6914824O/acsnano.6c16014.pdf?guestAccessKey=8de0abfb-c7d9-4588-addc-2b5c448d3cea by NANJING UNIV user on 12 November 2026

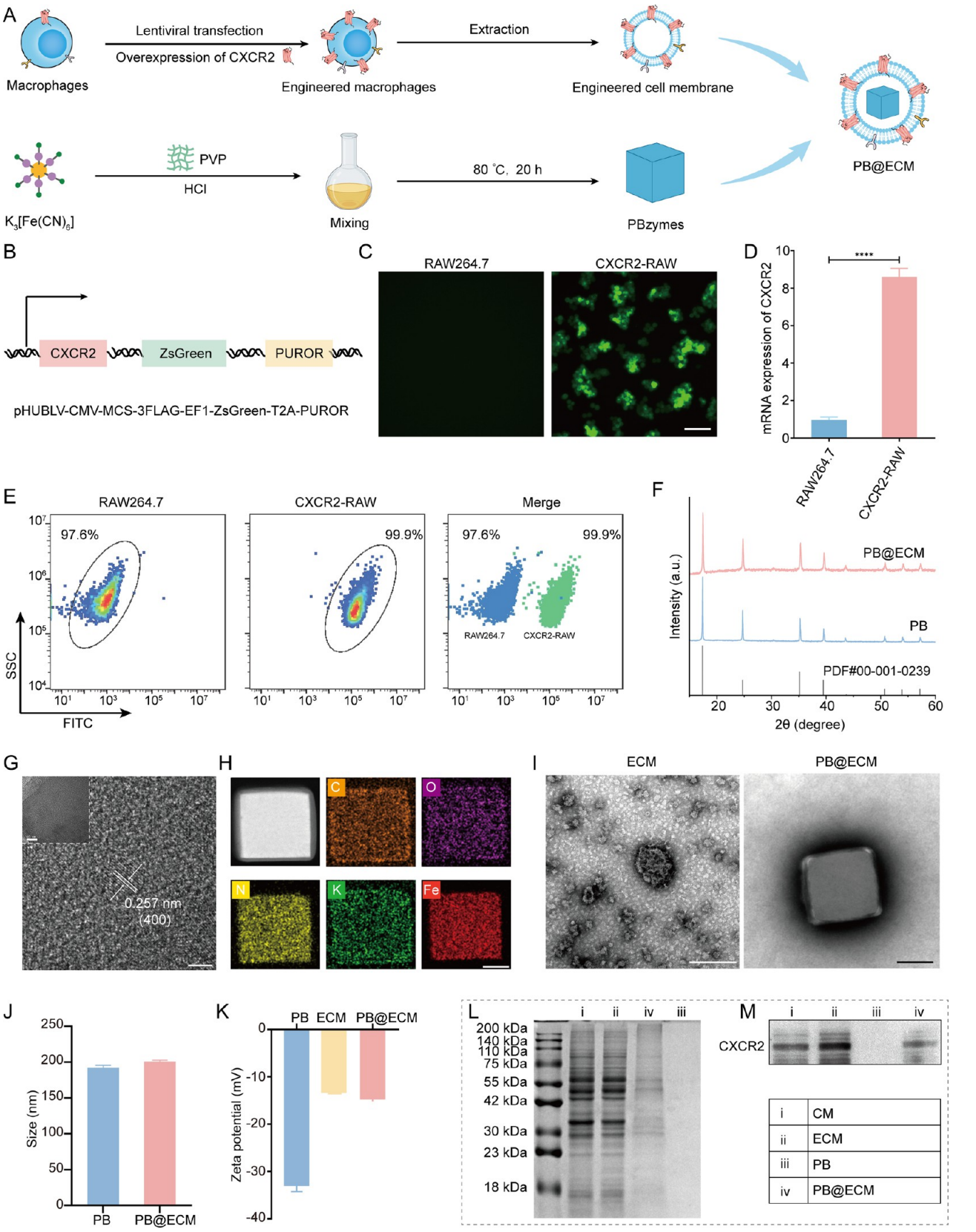


Figure 2. Characterization of PB@ECM. A, Schematic illustration of preparation of PB@ECM. B, Scheme of lentiviral vector encoding mouse CXCR2. ZsGreen, green fluorescent protein; PUROR, puromycin resistance gene encoding puromycin N-acetyltransferase. C, Representative fluorescence images of RAW264.7 and CXCR2-RAW cells, showing establishment of RAW264.7 cells stably expressing mouse CXCR2 on cell membranes (CXCR2-RAW). Left, normal RAW264.7 cells; Right, CXCR2-RAW cells. Scale bar, 50 μm. D, RT-qPCR analysis of *CXCR2* expression in RAW264.7 and CXCR2-RAW cells ($n = 3$). E, Representative flow cytometry analysis of green fluorescence protein in RAW264.7 and CXCR2-RAW cells. F, XRD patterns of PB and PB@ECM. Standard card, PDF#00-001-0239. G, HRTEM image of PB. Scale bar, 2 nm. Inset, low-resolution TEM

https://doi.org/10.1021/acsnano.6c16014
ACS Nano XXXX, XXX, XXX−XXX

Downloaded from pubs.acs.org/ancac3/article-pdf/doi/10.1021/acsnano.6c16014/6914824O/acsnano.6c16014.pdf?guestAccessKey=8de0abfb-c7d9-4588-addc-2b5c448d3cea by NANJING UNIV user on 12 November 2026

Figure 2. continued

image. Scale bar, 10 nm. H, EDS images of PB. Scale bar, 50 nm. I, TEM images of ECM and PB@ECM. Scale bar, 100 nm. J, Hydrodynamic diameters of PB and PB@ECM ($n = 3$). K, Zeta potentials of PB, ECM, and PB@ECM ($n = 3$). L, SDS-PAGE of CM, ECM, PB, and PB@ECM. M, Western blot of CXCR2 in CM, ECM, PB, and PB@ECM. CM, cell membrane of RAW264.7 cells; ECM, engineered cell membrane of CXCR2-RAW cells. ****$p < 0.0001$.

CAC (Figures 1B, C and S2E). Consistent with these transcriptomic findings, the enzyme-linked immunosorbent assay (ELISA) confirmed a trend toward higher CXCL2 secretion in colonic tissues from patients with IBD (Figure 1D). ELISA also confirmed significantly elevated CXCL2 secretion in colonic tissues from patients with CAC (Figure 1E). Gene Ontology (GO) analysis further indicated enhanced biological processes related to chemotaxis and migration of neutrophils and macrophages at lesion sites (Figure S2F).

To validate these observations and examine the correlation between CXCL2 and immune cell infiltration, we conducted further analysis using the disease database. Transcriptome data of IBD patients (GSE66407, Gene Expression Omnibus database) revealed a trend toward increased neutrophil infiltration and upregulated *CXCL2* expression in inflamed colonic tissue (Figures 1F and S3A). Correlation analysis confirmed positive associations between *CXCL2* expression and the infiltration of neutrophils and macrophages in IBD, with a more pronounced correlation for neutrophils (Figure 1G, H). As a general colon adenocarcinoma cohort used for cross-validation of CXCL2-CXCR2 axis activation in colorectal cancer, analysis of colon adenocarcinoma (COAD) patients' samples from The Cancer Genome Atlas Program (TCGA) database using Gene Expression Profiling Interactive Analysis (GEPIA)[22] revealed high *CXCL2* expression, associated with unfavorable relapse-free survival (Figures 1I and S3B). TISIDB[23] analysis also revealed a strong positive correlation between *CXCL2* expression and neutrophil infiltration in COAD patients (Figure 1J), whereas macrophage infiltration showed a weak negative correlation (Figure 1K). Together, these results indicated that *CXCL2* was positively correlated with neutrophil and macrophage infiltration during inflammation, but became more closely associated with neutrophil infiltration in tumors. Moreover, *CXCL2* expression positively correlated with *CXCR2* expression in both IBD and COAD tissues (Figure S3C, D), highlighting the involvement of the CXCL2-CXCR2 axis across disease stages.

Mechanistically, CXCL2 binds to CXCR2 on neutrophils and macrophages, recruiting them to sites of inflammation and tumors.[19,24−28] These immune cells release ROS and proinflammatory cytokines, which in turn exacerbate inflammation and promote tumorigenesis. Together, these findings suggested CXCL2-driven immune cell infiltration may contribute to the malignant transformation of chronic colitis to colorectal cancer. Therefore, targeting CXCL2 could represent a promising strategy to suppress immune cell infiltration and interrupt the inflammation-to-cancer transition in colonic diseases.

Preparation and Characterization of PB@ECM

Motivated by the above findings, we designed a biomimetic catalytic nanoformulation, termed "PB@ECM", by cloaking PB nanozymes with engineered cell membranes displaying CXCR2 (Figure 2A). This design enables competitive sequestration of CXCL2, the above-identified chemokine responsible for recruiting neutrophils and macrophages during inflammation and tumorigenesis. To generate the CXCR2-displaying membrane, the RAW264.7 macrophages were transduced with lentiviral vectors encoding CXCR2, together with Zoanthus green fluorescence protein (ZsGreen) and a 3 × Flag for selection and visualization (Figures 2B and S4). Following monoclonal screening, a stable CXCR2-overexpressing cell line (CXCR2-RAW) was established and validated by fluorescence microscopy, quantitative reverse transcription polymerase chain reaction (RT-qPCR), and flow cytometry (Figure 2C−E). Engineered cell membranes were isolated from CXCR2-RAW cells by lysis and differential centrifugation. In parallel, PB was synthesized according to established protocol,[29] exhibiting a uniform cubic morphology (Figures S5 and S6) and ferricyanide structure (Figure 2F). Subsequently, the ECM and PB were coextruded through 800 nm polycarbonate membranes to obtain PB@ECM. As a control, PB coated with native RAW264.7 cell membrane (PB@CM) was similarly prepared. High-resolution transmission electron microscope (HRTEM) revealed the lattice spacings of 0.257 nm corresponding to the (400) planes of PB (Figure 2G). High-angle annular dark-field scanning TEM (HAADF-STEM) and the corresponding energy-dispersive spectroscopy (EDS) elemental mappings of a PB nanocube confirmed a particle size of approximately 150 nm and a uniform distribution of Fe, C, N, O, and K elements (Figure 2H). TEM images of ECM vesicles exhibited a rounded cup-shaped structure, whereas PB@ECM showed a typical core−shell structure, in which the cubic PB core was surrounded with a membrane shell (Figures 2I and S7−S9). Dynamic light scattering (DLS) analysis indicated that the hydrodynamic diameter of PB@ECM (200.8 ± 1.1 nm) was slightly larger than that of uncoated PB nanocubes (191.0 ± 2.1 nm; Figures 2J and S10). The zeta potential of PB@ECM (−15.0 ± 0.1 mV) was comparable to that of ECM vesicles (−13.3 ± 0.1 mV), but less negative than that of uncoated PB cores (−33.2 ± 0.6 mV) (Figure 2K). Powder X-ray diffraction (PXRD) patterns of PB and PB@ECM exhibited the typical characteristic peaks of ferricyanide (Figure 2F), which confirmed that the PB retained their crystalline structure postcoating. X-ray photoelectron spectroscopy (XPS) analysis of Fe showed comparable profiles between PB and PB@ECM, indicating no alteration in PB's chemical state upon membrane coating (Figure S11). SDS-polyacrylamide gel electrophoresis (SDS-PAGE) and Western blot analysis further revealed that membrane proteins, including CXCR2, were preserved in PB@ECM (Figure 2L, M), implying successful membrane integration and functional retention from the parental CXCR2-RAW cells. Collectively, these results demonstrated the successful fabrication of PB@ECM, combining the catalytic activity of PB with the chemokine-sequestering capability of CXCR2-displaying membranes.

Enzyme-Like Catalytic Activity of PB@ECM

PB exhibits potent ROS-scavenging capabilities through multiple enzyme-like activities.[20] In this study, we systematically investigated the antioxidant activity of PB@ECM against representative ROS implicated in colitis pathogenesis, including superoxide anion ($O_2^{\bullet-}$), hydrogen peroxide (H_2O_2), and hydroxyl radicals ($^{\bullet}OH$). Next, we evaluated the enzyme-like

Downloaded from pubs.acs.org/ancac3/article-pdf/doi/10.1021/acsnano.6c16014/6914824O/acsnano.6c16014.pdf?guestAccessKey=8de0abfb-c7d9-4588-addc-2b5c448d3cea by NANJING UNIV user on 12 November 2026

https://doi.org/10.1021/acsnano.6c16014
ACS Nano XXXX, XXX, XXX−XXX

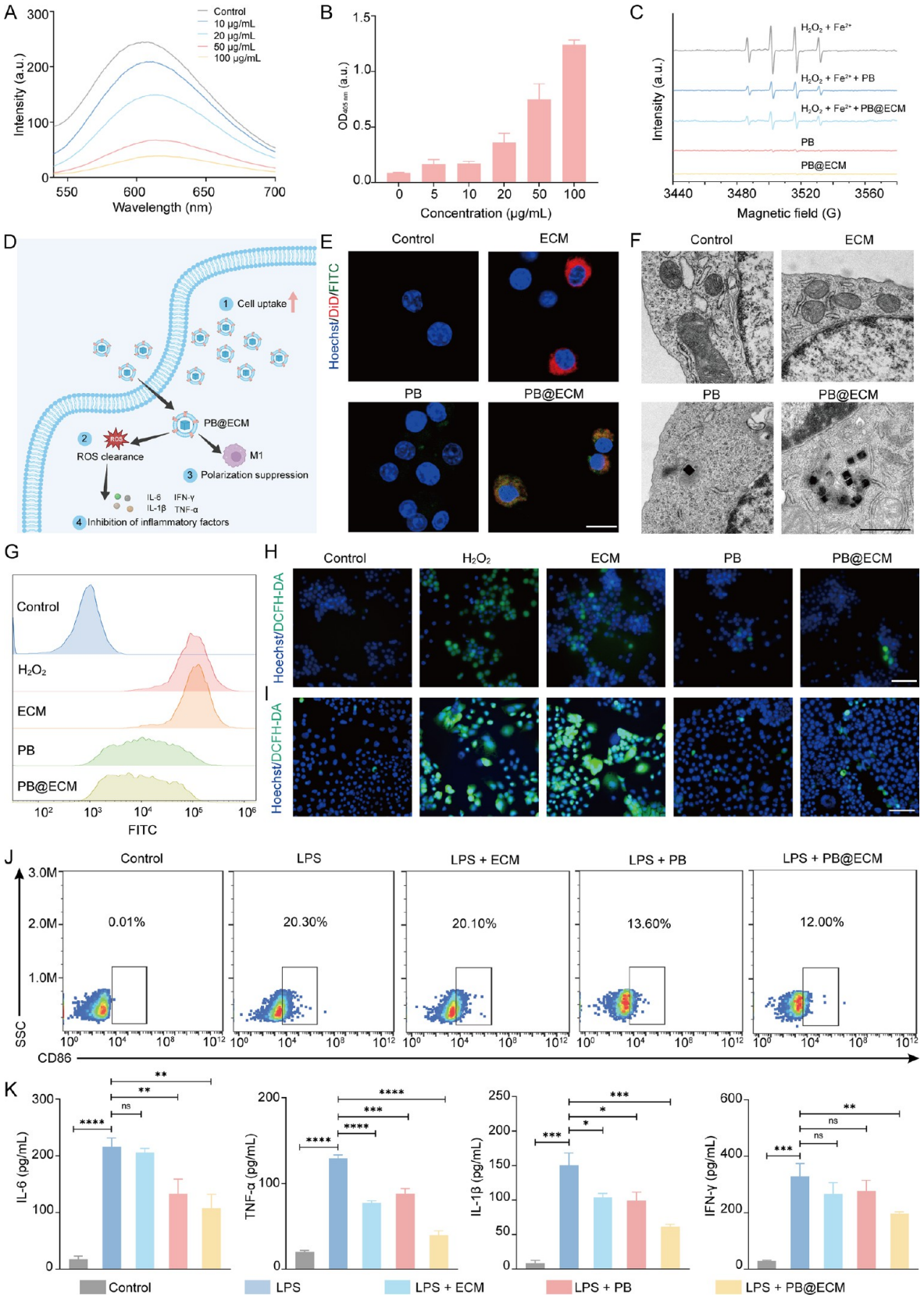


Figure 3. PB@ECM scavenges ROS and protects cells from oxidative stress. A, Fluorescence spectra for monitoring the reaction between HE, X, and XO in the absence and presence of PB@ECM. B, Quantitative bar chart of dopamine-enabled assay for CAT-like activity of PB@ECM (n = 3). C, Scavenging effect of PB and PB@ECM on •OH by EPR. D, Scheme of cellular effects of PB@ECM. E, Representative fluorescence images showing uptake of ECM, PB, and PB@ECM by RAW264.7 cells. ECM, DiD (red); PB, FITC (green); nuclei, Hoechst (blue). Scale bar, 20 μm. F, Representative TEM images showing location of PB and PB@ECM in RAW264.7 cells. Scale bar, 1 μm. G, Flow cytometry analysis of intracellular ROS levels in RAW264.7 cells treated with H_2O_2, H_2O_2 + ECM, H_2O_2 + PB, and H_2O_2 + PB@ECM. H, Confocal fluorescence images of ROS levels in

https://doi.org/10.1021/acsnano.6c16014
ACS Nano XXXX, XXX, XXX−XXX

Downloaded from pubs.acs.org/ancac3/article-pdf/doi/10.1021/acsnano.6c16014/6914824O/acsnano.6c16014.pdf?guestAccessKey=8de0abfb-c7d9-4588-addc-2b5c448d3cea by NANJING UNIV user on 12 November 2026

Figure 3. continued

RAW264.7 cells after indicated treatments. I, Confocal fluorescence images of ROS levels in Caco-2 cells after indicated treatments. ROS, DCFH-DA (green); nuclei, Hoechst (blue). Scale bar, 100 μm. J, Macrophage polarization of CD86 in RAW264.7 cells after indicated treatments, revealed by flow cytometry. K, Levels of typical inflammatory cytokines of RAW264.7 cells after indicated treatments ($n = 3$), including IL-6, TNF-α, IL-1β, and IFN-γ. ns, no significant difference, *$p < 0.05$, **$p < 0.01$, ***$p < 0.001$, ****$p < 0.0001$.

activities of PB@ECM to determine whether they were affected by ECM coating. To evaluate SOD-like activity, we employed dihydroethidium (DHE) fluorescence assays. PB@ECM treatment led to a concentration-dependent decrease in $O_2^{\bullet-}$ levels, indicating a superior $O_2^{\bullet-}$ scavenging ability (Figures 3A and S12A). These results were further confirmed using a commercial SOD assay kit (Figure S12B). CAT-like activity was assessed using a dopamine oxidation assay, wherein the decomposition of H_2O_2 generates O_2 that promotes the oxidative polymerization of dopamine. A significant increase in absorbance confirmed that PB@ECM efficiently catalyzed H_2O_2 breakdown in a dose-dependent manner (Figure 3B). Additionally, we employed electron paramagnetic resonance (EPR) spectroscopy to assess $^{\bullet}OH$ scavenging using 5,5-dimethyl-1-pyrroline *N*-oxide (DMPO) as a spin-trapping agent. A marked reduction in the EPR signal of the DMPO/$^{\bullet}OH$ adducts was observed upon treatment with PB@ECM, confirming its promising $^{\bullet}OH$-clearing ability (Figure 3C). Importantly, the ECM coating did not compromise the intrinsic catalytic activity of PB (Figure S13), indicating that the ROS-scavenging capability was well preserved after surface coating. Taken together, these results demonstrated the broad-spectrum ROS-scavenging activity of PB@ECM and underscored its potential for alleviating oxidative stress in colitis-associated inflammatory environments.

Intracellular ROS Scavenging and Anti-Inflammatory Capabilities of PB@ECM

The biocompatibility and cellular uptake of PB@ECM were evaluated to assess their therapeutic potential. First, the stability of PB@ECM was tested, and the results showed that it possessed good stability (Figure S14). Cytotoxicity assays demonstrated that PB@ECM possessed negligible toxicity toward RAW264.7 macrophages up to 100 μg/mL, comparable to pristine PB (Figure S15). Based on the activity test and cell membrane of PB@ECM, we next investigated its cellular functions (Figure 3D). To investigate cellular internalization, fluorescently labeled FITC-PB and FITC-PB@ECM were synthesized and subsequently incubated with RAW264.7 and Caco-2 cells (Figures S16 and S17). Confocal microscopy and TEM analysis revealed enhanced uptake of PB@ECM compared to PB (Figures 3E, F, S18, and S19), likely due to the ECM coating facilitating membrane interaction.[30]

To assess the cytoprotective potential of PB@ECM under oxidative stress, we established an *in vitro* inflammation model by treating RAW264.7 and Caco-2 cells with H_2O_2. Following PB@ECM treatment, intracellular ROS level was significantly reduced, as confirmed by DCFH-DA staining *via* both confocal microscopy and flow cytometry (Figure 3G–I), suggesting that PB@ECM efficiently scavenged ROS and alleviated oxidative stress. At the organelle level, TEM imaging revealed that PB@ECM preserved mitochondrial morphology under oxidative stress, preventing typical damage features such as swelling, matrix brightening, and cristae fragmentation (Figure S20). Moreover, PB@ECM exhibited robust anti-inflammatory effects. LPS was used to induce a pro-inflammatory phenotype in macrophages. Flow cytometric analysis indicated that PB@ECM inhibited M1 polarization of macrophages (Figure 3J), and ELISA measurements showed a marked reduction in pro-inflammatory cytokine secretion (Figure 3K). RT-qPCR analysis indicated that PB@ECM inhibited M1 markers (*Tnf, Nos2*) but had no significant effect on M2 markers (*Il10, Arg1*) (Figure S21). Collectively, these results demonstrated that PB@ECM effectively scavenged ROS, protected cells from oxidative damage, and modulated inflammatory response *in vitro*, supporting their promise for therapeutic applications in intestinal inflammation.

PB@ECM Sequesters CXCL2 and Inhibits Neutrophil and Macrophage Chemotaxis

To evaluate the CXCL2-sequestering capability of PB@ECM, we incubated CXCL2 with PB@CM or PB@ECM in the absence or presence of the CXCR2 antagonist SB225002. Only PB@ECM effectively sequestered CXCL2 (Figure 4A), owing to the expression of CXCR2 on the engineered membranes. This sequestration was diminished in the presence of SB225002, confirming the receptor–ligand specificity (Figure 4A). Based on the measured binding kinetic profiles, it was determined using the Hill equation that PB@ECM had an IC_{50} (half maximal inhibitory concentration) value of 39.68 μg/mL for CXCL2 binding (Figure S22). We next assessed whether CXCL2 sequestration could functionally suppress chemokine-driven immune cell migration using a transwell assay. Neutrophils were freshly isolated from murine bone marrow (Figure 4B). Neutrophils or RAW264.7 macrophages were placed in the upper chamber, while the lower chamber contained CXCL2 alone or in combination with PB, PB@CM, PB@ECM, or PB@ECM + SB225002 (Figure 4C). After 24 h, the number of migrated cells was quantified to assess chemotactic inhibition. PB@ECM exerted a much stronger inhibitory effect on neutrophil and macrophage migration compared with PB and PB@CM (Figure 4D–G). Notably, the inhibitory effect of PB@ECM was partially abrogated by SB225002, further substantiating that the antimigratory activity of PB@ECM was mediated by competitive CXCL2 binding through CXCR2 receptors on the engineered membrane (Figure 4D–G). To further examine the chemotactic modulation, a scratch-wound assay was performed to investigate the impact of PB@ECM on macrophage motility. PB@ECM exerted stronger inhibition of CXCL2-induced migration in RAW264.7 cells compared with PB, PB@CM, and PB@ECM treated with SB225002 (Figure 4H, I), indicating the essential role of CXCL2-CXCR2 interactions. Together, these results established PB@ECM as an effective chemokine scavenger capable of sequestering CXCL2 and attenuating neutrophil and macrophage chemotaxis. Beyond its intrinsic ROS-scavenging properties, the dual-functional nanoplatform PB@ECM offered a promising strategy for disrupting inflammatory cell recruitment within CXCL2-enriched microenvironments.

Therapeutic Effects of PB@ECM for Colitis

Given the potent ROS-scavenging capacity and chemotaxis-inhibitory properties of PB@ECM, we next assessed its therapeutic efficacy in a murine IBD model. Acute colitis was

Downloaded from pubs.acs.org/ancac3/article-pdf/doi/10.1021/acsnano.6c16014/6914824O/acsnano.6c16014.pdf?guestAccessKey=8de0abfb-c7d9-4588-addc-2b5c448d3cea by NANJING UNIV user on 12 November 2026

https://doi.org/10.1021/acsnano.6c16014
ACS Nano XXXX, XXX, XXX–XXX

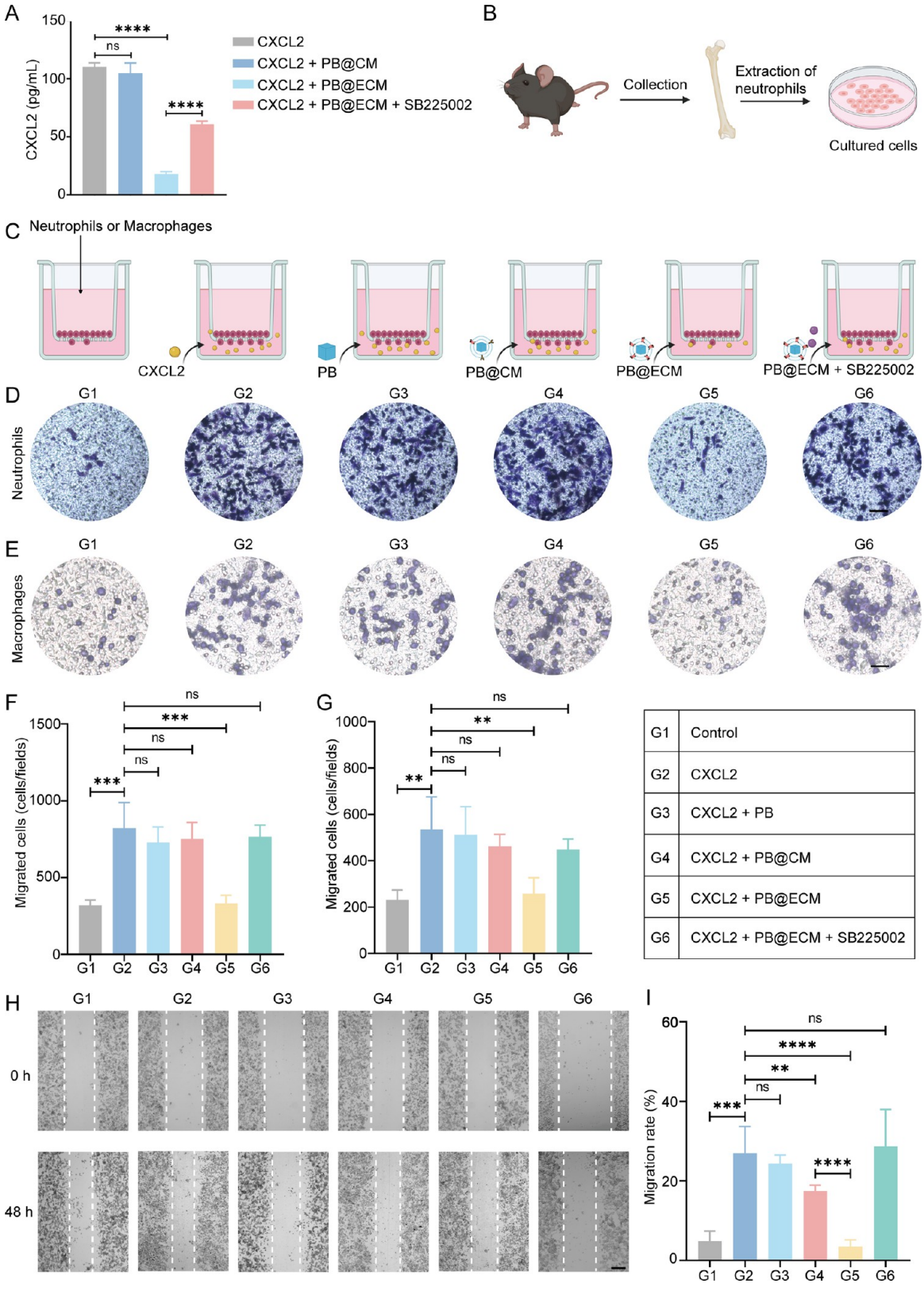


Figure 4. *In vitro* inhibition of neutrophil and macrophage migration by PB@ECM *via* CXCL2-CXCR2 axis. A, Content of CXCL2 in supernatant after incubation of CXCL2 solution with PB@CM, PB@ECM, and PB@ECM + SB225002, measured by ELISA (n = 3). B, Schematic illustration of neutrophil extraction from mouse bone marrow. C, Schematic illustration of transwell experiment. Representative images (D) and quantification (F) of migratory neutrophil cells stained with crystal violet at 24 h after incubation with CXCL2, CXCL2 + PB, CXCL2 + PB@CM, CXCL2 + PB@ECM, and CXCL2 + PB@ECM + SB225002, determined by transwell assay (n = 5). Scale bar, 50 μm. Representative images (E) and quantification (G) of migratory RAW264.7 cells stained with crystal violet at 24 h after incubation with CXCL2, CXCL2 + PB, CXCL2 + PB@CM, CXCL2 + PB@ECM, and CXCL2 + PB@ECM + SB225002, determined by transwell assay (n = 5). Scale bar, 50 μm. Representative images (H) and quantification (I) of

https://doi.org/10.1021/acsnano.6c16014
ACS Nano XXXX, XXX, XXX−XXX

Downloaded from pubs.acs.org/ancac3/article-pdf/doi/10.1021/acsnano.6c16014/6914824O/acsnano.6c16014.pdf?guestAccessKey=8de0abfb-c7d9-4588-addc-2b5c448d3cea by NANJING UNIV user on 12 November 2026

Figure 4. continued

migratory RAW264.7 cells at 48 h after incubation with CXCL2, CXCL2 + PB, CXCL2 + PB@CM, CXCL2 + PB@ECM, and CXCL2 + PB@ECM + SB225002 (n = 5). Scale bar, 200 μm. ns, no significant difference, **p < 0.01, ***p < 0.001, ****p < 0.0001.

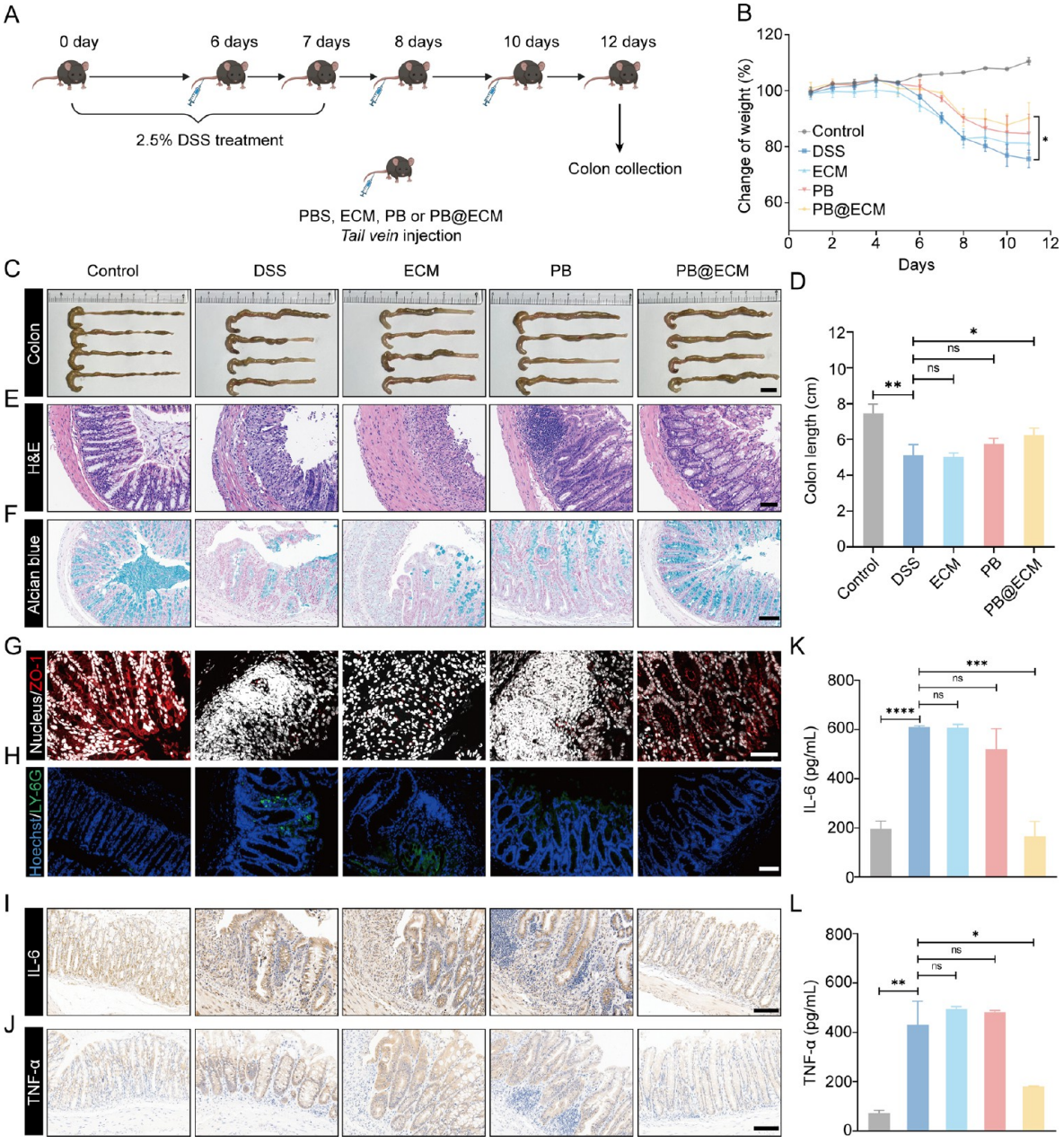


Figure 5. Anti-inflammatory activity and inhibition of neutrophil and macrophage infiltration by PB@ECM in DSS-induced mice. A, Schematic illustration of DSS-induced mouse model. B, Daily body weight changes of mice for 11 days. C, Photographs of colons and (D) corresponding colon lengths after indicated treatments (n = 4). Scale bar, 1 cm. E, H&E-stained colonic sections after indicated treatments. Scale bar, 100 μm. F, Alcian blue-stained colonic sections after indicated treatments. Scale bar, 100 μm. G, Immunofluorescence images of ZO-1 in colon tissues. Scale bar, 50 μm. Representative confocal images of neutrophil (H) in colon tissues. Neutrophil, LY-6G (green); nucleus, Hoechst (blue). Scale bar, 100 μm. Immunohistochemistry images of IL-6 (I) and TNF-α (J) in colon tissues. Scale bar, 100 μm. Levels of IL-6 (K) and TNF-α (L) in colons on day 12 after indicated treatments by ELISA (n = 3). ns, no significant difference, *p < 0.05, **p < 0.01, ***p < 0.001, ****p < 0.0001.

induced in C57BL/6 mice by administering 2.5% (w/v) DSS (dextran sodium sulfate) in drinking water for 7 days, followed by tail vein injections of PBS, ECM, PB, or PB@ECM on days 6, 8, and 10, as outlined in Figure 5A. Body weight changes, a key indicator of colitis progression, were monitored throughout the study (Figure 5B). DSS-induced colitis led to a 23.5% reduction in body weight, whereas healthy controls displayed continuous weight gain. Notably, treatment with PB@ECM significantly ameliorated weight loss, with only a 10.5% reduction, compared to 15.0% in the PB-treated group (Figure 5B). Additionally, PB@ECM treatment effectively mitigated DSS-induced colon shortening, a hallmark of intestinal inflammation, outperforming

https://doi.org/10.1021/acsnano.6c16014
ACS Nano XXXX, XXX, XXX−XXX

Downloaded from pubs.acs.org/ancac3/article-pdf/doi/10.1021/acsnano.6c16014/6914824O/acsnano.6c16014.pdf?guestAccessKey=8de0abfb-c7d9-4588-addc-2b5c448d3cea by NANJING UNIV user on 12 November 2026

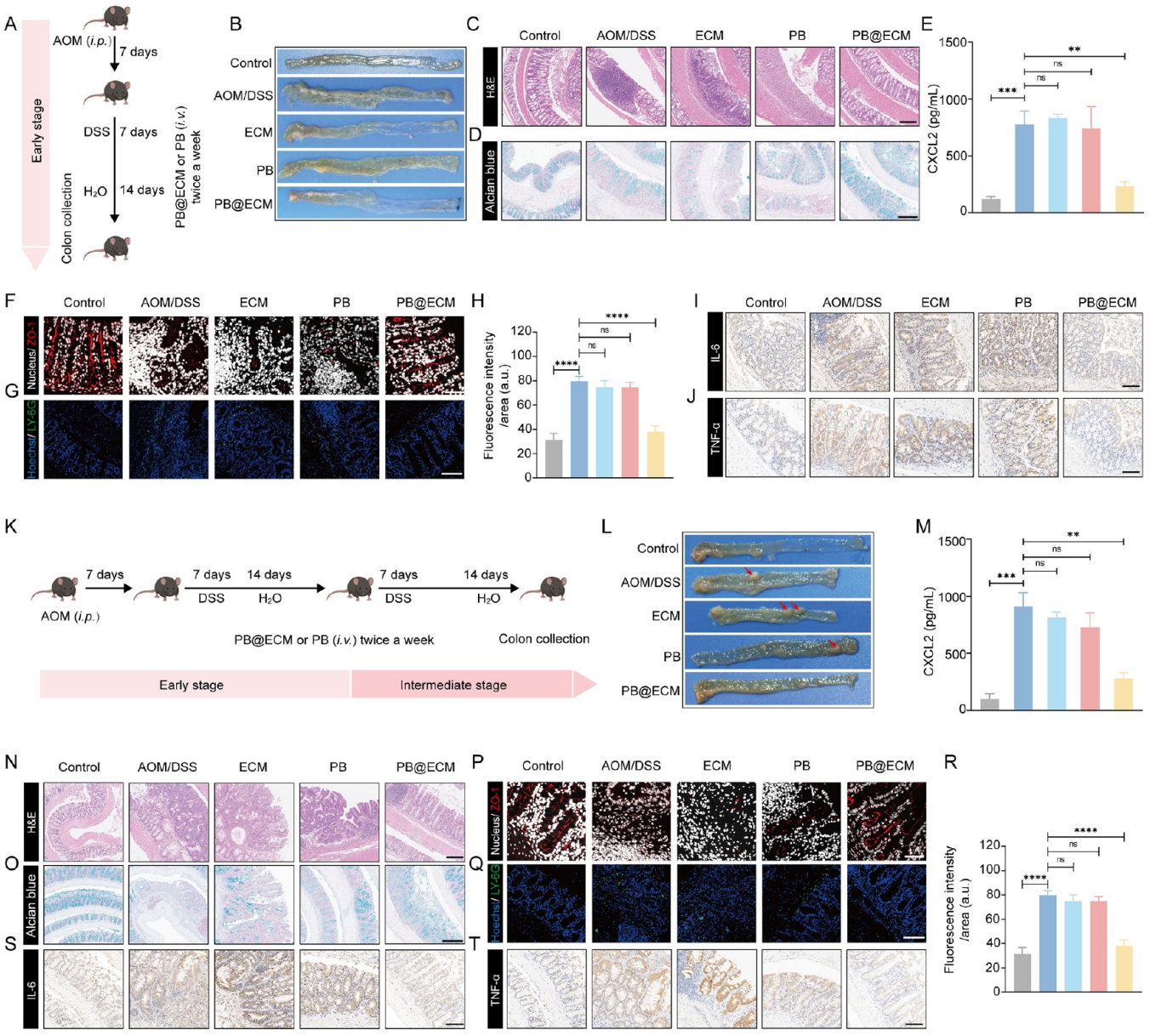


Figure 6. Treatment of preliminary stage CAC mice with PB@ECM. A, Schematic illustration for PB@ECM treatment of AOM/DSS mice (early stage). B, Representative photographs of colons from Control, ECM, PB, and PB@ECM groups at early stage. Representative H&E (C) and alcian blue (D)-stained colonic sections from Control, AOM/DSS, ECM, PB, and PB@ECM groups at early stage. Scale bar, 200 μm. E, ELISA of CXCL2 in colons at early stage (n = 3). F, Immunofluorescence images of ZO-1 in colon tissues of early stage. Scale bar, 50 μm. G, Representative confocal images of neutrophil in colon tissue at early stage. Neutrophil, LY-6G (green); nucleus, Hoechst (blue). Scale bar, 100 μm. H, Quantitative analysis of LY-6G immunofluorescence staining (n = 4). Immunohistochemistry images of IL-6 (I) and TNF-α (J) in colon tissues. Scale bar, 100 μm. K, Schematic illustration for PB@ECM treatment of AOM/DSS mice (intermediate stage). L, Representative photographs of colons from Control, ECM, PB, and PB@ECM groups at intermediate stage. M, ELISA of CXCL2 in colons at intermediate stage (n = 3). Representative H&E (N) and alcian blue (O)-stained colonic sections from Control, AOM/DSS, ECM, PB, and PB@ECM groups at intermediate stage. Scale bar, 200 μm. P, IF images of ZO-1 in colon tissues of intermediate stage. Scale bar, 50 μm. Q, Representative confocal images of neutrophil in colon tissue at intermediate stage. Neutrophil, LY-6G (green); nucleus, Hoechst (blue). Scale bar, 100 μm. R, Quantitative analysis of LY-6G immunofluorescence staining (n = 4). Immunohistochemistry images of IL-6 (S) and TNF-α (T) in colon tissues. Scale bar, 100 μm. ns, no significant difference, *p < 0.05, **p < 0.01, ***p < 0.001.

the PB and ECM groups (Figure 5C and D). Histological analysis further corroborated these findings. Hematoxylin and eosin (H&E) and alcian blue (AB) staining revealed that DSS treatment caused marked disruption of the colonic architecture, mucus barrier, and epithelial integrity. Treatment with PB@ECM substantially mitigated these pathological changes, showing superior tissue preservation and reduced inflammatory cell infiltration compared to other treatment groups (Figure 5E and F). The intact epithelial barrier is the basic premise for intestinal health and normal physiological function. ZO-1 is a major intestinal tight junction protein closely associated with intestinal barrier integrity. The immunofluorescence assay showed that PB@ECM notably improved the expression levels of ZO-1 in the colitis colon compared to the other groups (Figure 5G). These findings indicated the superior capacity of PB@ECM in alleviating DSS-induced systemic symptoms.

https://doi.org/10.1021/acsnano.6c16014
ACS Nano XXXX, XXX, XXX−XXX

Downloaded from pubs.acs.org/ancac3/article-pdf/doi/10.1021/acsnano.6c16014/6914824O/acsnano.6c16014.pdf?guestAccessKey=8de0abfb-c7d9-4588-addc-2b5c448d3cea by NANJING UNIV user on 12 November 2026

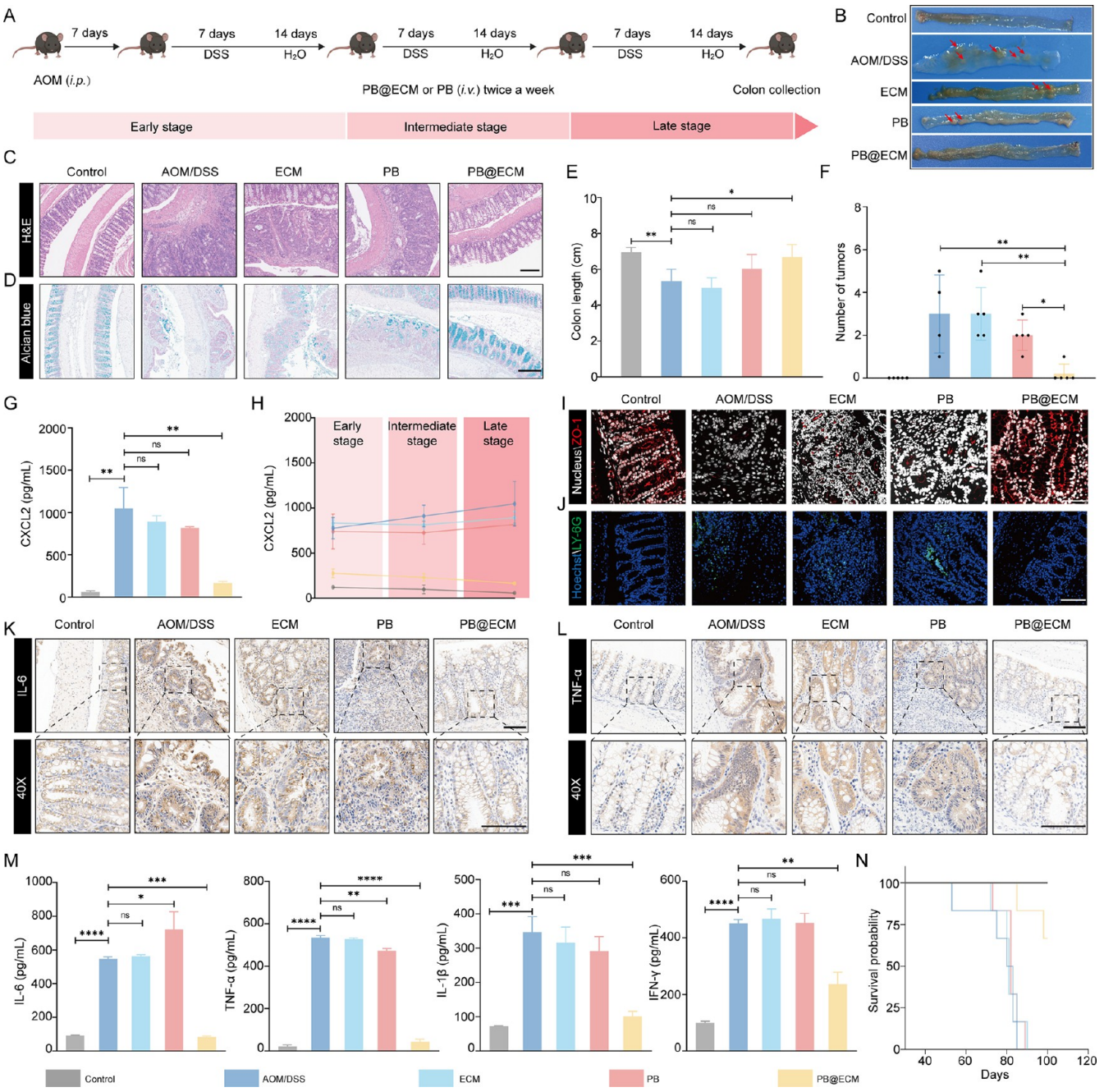


Figure 7. Treatment of late-stage CAC mice with PB@ECM. A, Schematic illustration for PB@ECM treatment of AOM/DSS mice (late stage). B, Representative photographs of colons from Control, ECM, PB, and PB@ECM groups at late stage. Representative H&E (C) and alcian blue (D)-stained colonic sections from Control, AOM/DSS, ECM, PB, and PB@ECM groups at late stage. Scale bar, 200 μm. E, Colon lengths in indicated groups at late stage ($n = 5$). F, Number of tumors in indicated groups at late stage ($n = 5$, n (AOM/DSS) = 4). The incidence was 20% in the PB@ECM group versus 100% in the AOM/DSS, ECM, and PB groups. G, ELISA of CXCL2 in colons at late stage ($n = 3$). H, Changes of CXCL2 at three different stages ($n = 3$). I, Immunofluorescence images of ZO-1 in colon tissues of late stage. Scale bar, 50 μm. J, Representative confocal images of neutrophil in colon tissue at late stage. Neutrophil, LY-6G (green); nucleus, Hoechst (blue). Scale bar, 100 μm. Immunohistochemistry images of IL-6 (K) and TNF-α (L) in colon tissues. Scale bar, 100 μm. M, ELISA of IL-6, TNF-α, IL-1β, and IFN-γ in colons at late stage ($n = 3$). N, Survival rate analysis of CAC mice ($n = 6$). ns, no significant difference, *$p < 0.05$, **$p < 0.01$, ***$p < 0.001$.

Furthermore, PB@ECM-treated mice exhibited markedly reduced neutrophil and macrophage infiltration in colonic tissues compared to other treatment groups (Figures 5H and S23). The results of immunohistochemistry showed that PB@ECM significantly reduced the levels of IL-6 and TNF-α proteins in the inflammatory sites (Figure 5I and J). ELISA results revealed that PB@ECM significantly lowered the levels of key proinflammatory cytokines, including IL-6, TNF-α, IL-1β, and IFN-γ (Figures 5K, L and S24). These findings suggested that the superior therapeutic efficacy of PB@ECM arose from its combined ability to attenuate inflammation and suppress immune cell accumulation in the colon.

PB@ECM Inhibits Colitis to Colitis-Carcinoma Progression

CAC develops from chronic IBD, driven by sustained oxidative stress and immune cell infiltration. IBD lesions feature elevated

https://doi.org/10.1021/acsnano.6c16014
ACS Nano XXXX, XXX, XXX−XXX

Downloaded from pubs.acs.org/ancac3/article-pdf/doi/10.1021/acsnano.6c16014/6914824/acsnano.6c16014.pdf?guestAccessKey=8de0abfb-c7d9-4588-addc-2b5c448d3cea by NANJING UNIV user on 12 November 2026

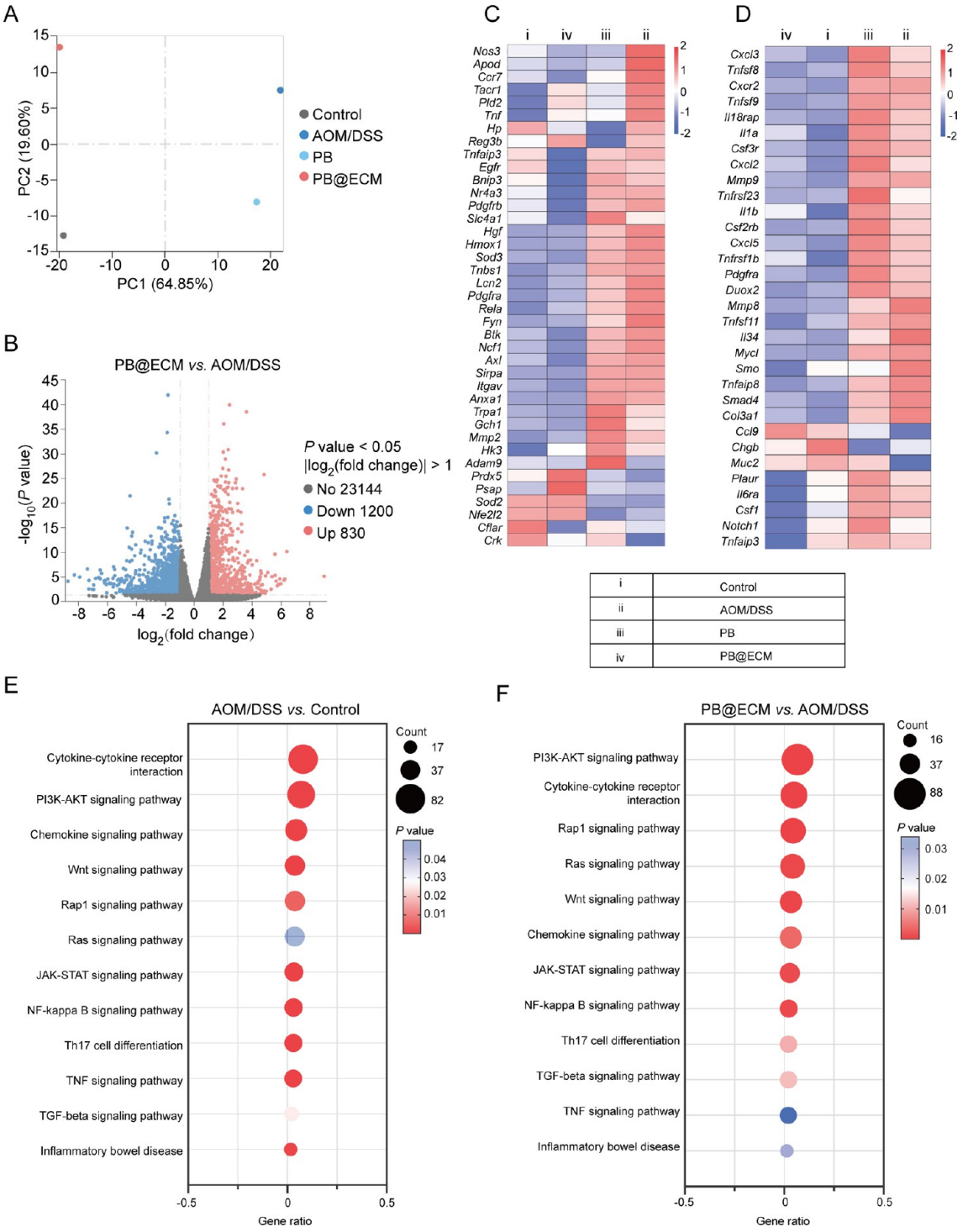


Figure 8. Transcriptome sequencing analysis of treatment with PB@ECM. A, Principal component analysis showed diversity of different groups (n = 3). B, Volcano plots of differential expression analysis (DEGs) in AOM/DSS and PB@ECM groups (|fold change| ≥ 2.0; $p < 0.05$; up-regulated genes: red; down-regulated genes: blue). Heatmap of DEGs related to ROS (C) and tumor occurrence (D). KEGG pathways enriched among genes upregulated in AOM/DSS group compared to Control group (E) and down-regulated genes in PB@ECM-treated group versus AOM/DSS group (F). PI3K-AKT, Phosphatidylinositol 3-Kinase/Akt pathway; JAK-STAT, Janus kinase−signal transducers and activators of transcription; Rap1, Ras-proximate-1; Wnt, Wingless/Integration; TNF, Tumor necrosis factor; NF-kappa B, Nuclear factor kappa-light-chain-enhancer of activated B cells.

ROS and CXCL2 levels, which together promote epithelial damage and recruit neutrophils and macrophages, accelerating the inflammation-to-cancer transition. Our *in vitro* studies confirmed that the PB@ECM catalytic nanoformulation both scavenged ROS and disrupted CXCL2 activity, highlighting its potential to impede CAC progression.

To evaluate the therapeutic benefits of PB@ECM in CAC, we first assessed its targeting ability *in vivo*. After establishing the CAC model using AOM/DSS (AOM, azoxymethane), FITC-PB and FITC-PB@ECM were intravenously injected on day 29, and colons were harvested 6 h postinjection for fluorescence analysis (Figure S25A, B). As shown in Figures S25C, D and

https://doi.org/10.1021/acsnano.6c16014
ACS Nano XXXX, XXX, XXX−XXX

Downloaded from pubs.acs.org/ancac3/article-pdf/doi/10.1021/acsnano.6c16014/6914824O/acsnano.6c16014.pdf?guestAccessKey=8de0abfb-c7d9-4588-addc-2b5c448d3cea by NANJING UNIV user on 12 November 2026

S26, FITC-PB@ECM exhibited significantly higher accumulation in the colon compared with FITC-PB (11.88×10^9 vs 3.99×10^9 (p/s)/(μW/cm^2)), attributed to the inflammatory targeting capability of the ECM. Then, we monitored the biodistribution of FITC-labeled PB@ECM at 12, 24, 36, and 48 h after intravenous injection using *in vivo* imaging. The results showed that fluorescence in the inflamed colon peaked at 12 h and then gradually decreased, becoming nearly undetectable at 48 h. Strong fluorescence was observed in the liver and kidneys compared with other organs, indicating that PB@ECM is cleared primarily through hepatobiliary and renal routes, with the liver being the major clearance organ (Figures S27 and S28). Given the differences between etched porous PB and unetched PB, which may affect *in vivo* behavior, to address this concern directly, we performed ICP-OES (Inductively Coupled Plasma Optical Emission Spectrometer) quantification of Fe using the unetched PB@ECM therapeutic formulation itself, thereby avoiding the use of etched PB for biodistribution analysis. Fe accumulation in the inflamed colon peaked at approximately 12 h and then gradually decreased. By 48 h, Fe levels in most tissues had returned to near baseline, indicating that PB@ECM is largely cleared from the body within 48 h. The liver and kidneys showed higher Fe levels than other organs, indicating that PB@ECM is mainly cleared through hepatic and renal pathways (Figure S29). The above results indicate that PB@ECM possesses excellent inflammatory targeting properties.

The therapeutic efficacy of PB@ECM was then evaluated across three stages of disease progression. In the early stage (Figure 6A), no significant differences in colon length or visible tumor formation were observed among the ECM, PB, and PB@ECM groups (Figures 6, S30A, and S31). However, histological analysis revealed markedly alleviated colonic inflammation barrier damage in the PB@ECM group (Figure 6C, D). The immunofluorescence assay showed that PB@ECM notably improved the expression levels of ZO-1 in the colitis colon compared to the other groups (Figure 6F). Additionally, reduced neutrophil and macrophage infiltration was observed by immunofluorescence analysis, accompanied by decreased CXCL2 levels in the colon (Figures 6E−H and S30B, C). The results of immunohistochemistry showed that PB@ECM significantly reduced the levels of IL-6 and TNF-α proteins in the inflammatory sites (Figure 6I, J). And cytokine profiling further showed that PB@ECM-treated mice had significantly lower levels of IL-6, TNF-α, IL-1β, and IFN-γ compared to the AOM/DSS, ECM, and PB groups (Figure S30D−G), indicating its efficacy in mitigating early inflammatory injury.

In the intermediate stage (Figure 6K), although colon length remained comparable across groups (Figures S32A and S33A), PB@ECM-treated mice did not develop tumor areas, unlike the AOM/DSS, ECM, and PB groups (Figures 6L and S33B). Histological analysis revealed markedly inhibited tumor formation and protected the mucosal barrier in the PB@ECM group compared to the AOM/DSS, ECM, and PB groups (Figure 6N, O, and P), indicating its efficacy in mitigating colitis to tumorigenesis. Importantly, neutrophil and macrophage infiltration was substantially mitigated in the PB@ECM group due to the reduced CXCL2 levels, which also maintained lower cytokine levels (Figures 6M, Q, R and S32B, C). PB@ECM continuously reduced the levels of IL-6 and TNF-α proteins in the inflammatory sites (Figure 6S, T). Cytokine profiling further showed that PB@ECM-treated mice had significantly lower levels of IL-6, TNF-α, IL-1β, and IFN-γ compared to the other groups (Figure S32D−G). These results suggest that PB@ECM effectively limited disease progression from colitis to tumor.

By the late stage (Figure 7A), the therapeutic advantages of PB@ECM became increasingly pronounced. Notably, some PB@ECM-treated mice exhibited a complete absence of detectable tumors (Figures 7B and S34B). H&E and alcian blue staining revealed minimal mucosal injury and leukocyte infiltration. Histological analysis revealed markedly inhibited tumor formation and protected the mucosal barrier in the PB@ECM group (Figure 7C, D). PB@ECM treatment significantly attenuated colon shortening (Figures 7E and S34A) and markedly reduced tumor burden relative to ECM, PB, and untreated groups (Figures 7F and S34B). ELISA results of the PB@ECM group confirmed sustained suppression of CXCL2 in the colon (Figure 7G). Remarkably, CXCL2 levels in the PB@ECM group remained consistently low across all three disease stages, with no significant difference compared to the healthy controls (Figure 7H). Immunofluorescence assay showed that PB@ECM notably improved the expression levels of ZO-1 in the colitis colon compared to the other groups (Figure 7I). Immunofluorescence analysis further demonstrated significantly reduced infiltration of neutrophils and macrophages (Figure 7J and S35), in line with decreased CXCL2 expression. The results of immunohistochemistry showed that PB@ECM significantly reduced the levels of IL-6 and TNF-α proteins in the inflammatory sites (Figure 7K, L). ELISA results of the PB@ECM group confirmed sustained suppression of proinflammatory cytokines in the colon (Figure 7M). The immunohistochemistry of Ki67 showed that during the CAC process, the treatment with PB@ECM significantly inhibited the proliferation of cells in the colon region and reduced the risk of deterioration (Figure S36). Compared with other groups, the treatment with PB@ECM significantly prolonged the survival of CAC mice (Figure 7N). DHE-stained fluorescence images of the colon (Figure S37) demonstrated that the PB@ECM inhibited colon oxidative stress. These findings highlighted the dual therapeutic effects of PB@ECM in attenuating inflammation and limiting immune cell infiltration, thereby effectively impeding the colitis-to-cancer transition.

Further histological analysis of major organs (heart, liver, spleen, lung, and kidney) revealed no signs of systemic toxicity across all treatment groups (Figures S38−S40), supporting the favorable biosafety profile of PB@ECM.

Transcriptomic Profiling of PB@ECM-Treated CAC Mouse Colons

To elucidate the mechanisms underlying the therapeutic effects of PB@ECM, we performed transcriptomic analysis on colonic tissues from late-stage CAC mice. Principal component analysis revealed distinct transcriptomic profiles among the Control, AOM/DSS, PB, and PB@ECM groups (Figure 8A), indicating marked immune microenvironment remodeling upon treatment. Venn diagram analysis further illustrated differentially expressed gene patterns across key comparisons, including AOM/DSS vs Control, PB@ECM vs PB, and PB@ECM vs AOM/DSS groups (Figure S41). Specifically, volcano plots identified 973 up-regulated and 861 down-regulated genes in the AOM/DSS group compared to the Control group (Figure S42A), while PB@ECM treatment resulted in 637 up-regulated and 1299 down-regulated genes relative to the PB group (Figure S42B). Notably, PB@ECM significantly altered 2030 transcripts compared to the AOM/DSS group, including 830 up-regulated

Downloaded from pubs.acs.org/ancac3/article-pdf/doi/10.1021/acsnano.6c16014/6914824O/acsnano.6c16014.pdf?guestAccessKey=8de0abfb-c7d9-4588-addc-2b5c448d3cea by NANJING UNIV user on 12 November 2026

https://doi.org/10.1021/acsnano.6c16014
ACS Nano XXXX, XXX, XXX−XXX

and 1200 down-regulated genes, based on the filtering criteria of |fold change| ≥ 2.0 and $p < 0.05$ (Figure 8B).

A heatmap of selected genes revealed a prominent down-regulation of pathways associated with ROS response, inflammatory signaling, and tumorigenesis following PB@ECM treatment (Figures 8C, D and S43). Kyoto Encyclopedia of Genes and Genomes (KEGG) pathway enrichment analysis further demonstrated that PB@ECM treatment significantly suppressed pathways associated with immune activation and oncogenic pathways, including cytokine−cytokine receptor interaction, chemokine signaling, PI3K-AKT, Rap1, Wnt, JAK-STAT, and NF-κB signaling cascades (Figure 8E, F). Consistently, gene set enrichment analysis (GSEA) demonstrated a down-regulation of tumor-promoting signaling pathways upon PB@ECM treatment, including PI3K-AKT, TGF-β, and TNF (Figure S44). GO analysis further indicated that PB@ECM down-regulated genes involved in leukocyte migration and activation, such as those regulating neutrophil chemotaxis, macrophage activation, and general cell migration (Figure S45). These transcriptomic changes reflected PB@ECM's capacity to sequester CXCL2 and thereby limit recruitment of neutrophils and macrophages, the effect also supported by ELISA measurement and immunofluorescence staining (Figures 7G, J and S35). Collectively, these findings suggested that PB@ECM conferred therapeutic benefit by dampening inflammation, mitigating oxidative stress, and inhibiting immune cell infiltration and pro-tumor signaling, ultimately halting the progression of colitis into colorectal cancer.

CONCLUSIONS

Nanozymes have emerged as powerful platforms for biomedical applications owing to their catalytic robustness and multifunctionality.[31−33] Antioxidant nanozymes, in particular, have shown promise in treating inflammation-driven diseases by mitigating excessive ROS,[34] including IBD[35−37] and cardiovascular diseases.[38,39] However, chronic inflammatory microenvironments are governed not only by oxidative stress but also by persistent immune cell infiltration and chemokine signaling, which together accelerate tissue damage and malignant transformation. The inability of single-functional nanozymes to simultaneously address these interconnected pathological cues has limited their efficacy in intercepting inflammation-to-cancer progression.[40,41]

In this study, we report PB@ECM, a biomimetic nanozyme that integrates catalytic antioxidant activity with targeted chemokine sequestration to reprogram inflammatory immune niches. The PB core efficiently scavenges ROS *via* SOD- and CAT-like activities, while the genetically engineered macrophage membrane coating neutralizes CXCL2 through overexpressed CXCR2, thereby suppressing excessive neutrophil and macrophage recruitment. By concurrently attenuating oxidative injury and immune chemotaxis, PB@ECM disrupts the self-amplifying inflammatory cascade that drives CAC. Compared with PB or ECM alone, PB@ECM exhibits dual therapeutic efficacy, markedly reducing inflammation, immune infiltration, and tumor burden across multiple stages of disease progression.

Importantly, PB@ECM leverages clinically relevant components, as PB is FDA-approved and cell membranes are inherently biocompatible,[42,43] underscoring its translational potential. Future studies should focus on optimizing administration routes, validating efficacy and safety in large animal models, and benchmarking against established anti-inflammatory therapies. We also made a simple comparison of our work with other treatment methods (Tables S6 and S7). Overall, this work establishes a dual therapeutic efficacy biomimetic nanozyme paradigm for intercepting inflammation-driven carcinogenesis. Beyond CAC, the modular integration of enzyme-mimicking cores with engineered membranes offers a broadly applicable strategy for reprogramming pathological immune microenvironments and preventing inflammation-associated malignancies. We also acknowledge that this design is limited by its focus on the CXCL2-CXCR2 axis and by batch variability, stability, and scale-up challenges of the engineered membrane. And the long-term immunogenicity/safety and relative *in vivo* contributions of antioxidant versus chemokine-neutralizing effects require further investigation.

METHODS/EXPERIMENTAL

Synthesis of PB@ECM

0.5 mL of PB solution (1 mg/mL) was mixed with 0.5 mL of ECM (~6 × 10^6 cells/mL) in PBS (pH 7.4), and then coextruded through a 0.8 μm polycarbonate membrane with a miniextruder (Avanti Polar Lipids, USA) for 13 times to get the PB@ECM nanocomposites. The samples were stored at −80 °C for further use.

Regarding the stability of PB@ECM, PB@ECM was dispersed in (i) deionized water, (ii) 1× PBS (pH 7.4), and (iii) DMEM containing 10% FBS. Samples were incubated at 37 °C, and hydrodynamic diameter and zeta potential were measured at 0, 2, 4, 6, 8, 10, 12, and 14 days by dynamic light scattering (DLS).

Measurement of SOD-Like Activity

HE, an $O_2^{\bullet-}$ fluorescence probe, was used to assess the amount of $O_2^{\bullet-}$. The SOD-like activity of PB and PB@ECM was evaluated by measuring the amount of $O_2^{\bullet-}$ with the HE probe. Typically, different concentrations of PB and PB@ECM, xanthine (0.5 mM), and xanthine oxidase (0.05 U/mL) were mixed in Tris-HCl buffer (0.1 M, pH 7.4) at 37 °C for 30 min. HE (0.5 mg/mL) was added to the solution for another 30 min reaction. Then, the fluorescence spectra were recorded, with excitation and emission wavelengths of 470 and 610 nm, respectively.

The SOD-like activity of PB and PB@ECM was also assessed by using a SOD assay kit. First, 20 μL of the sample was mixed with 200 μL of 2-(4-iodophenyl)-3-(4-nitrophenyl)-5-(2,4-disulfophenyl)-2H-tetrazolium, monosodium salt. Next, 20 μL of the enzyme working solution was added to the mixture and incubated at 37 °C for 20 min. Finally, the absorbance at 450 nm was recorded by using a microplate reader.

Measurement of Hydroxyl Radical Scavenging Activity *via* EPR

EPR spectra were used to measure the hydroxyl radical ($^{\bullet}OH$) scavenging activity. Hydroxyl radicals were generated by the reaction of H_2O_2 and Fe^{2+}, which can be captured by DMPO. The sample contained a final concentration of H_2O_2 (0.5 mM), Fe^{2+} (5 μM), nanozyme (0.1 mg/mL), and DMPO (22.5 mg/mL) in PBS buffer (pH = 7.4). After adding Fe^{2+} to start the reaction for 2 min, the nanozyme was added to react for 60 s, and the EPR spectra were immediately recorded.

Cell Culture

The mouse macrophage cell line RAW264.7 and the human colon cancer cell line Caco-2 were purchased from the Cell Bank of Type Culture Collection of Chinese Academy of Sciences (Shanghai, China). The RAW264.7 cells and Caco-2 cells were maintained in DMEM supplemented with 10% (v/v) fetal bovine serum (FBS) and 1% (v/v) antibiotics. All the cells were maintained at 37 °C in a humidified incubator with 5% CO_2.

Study Approval

Collection and measurement of human samples were approved by the Medical Ethics Committee of Jinling Hospital (2023DZKY-001-01) and informed consent was obtained from all participants. The samples

Downloaded from pubs.acs.org/ancac3/article-pdf/doi/10.1021/acsnano.6c16014/6914824O/acsnano.6c16014.pdf?guestAccessKey=8de0abfb-c7d9-4588-addc-2b5c448d3cea by NANJING UNIV user on 12 November 2026

https://doi.org/10.1021/acsnano.6c16014
ACS Nano XXXX, XXX, XXX−XXX

were taken from the lesion tissue and the adjacent normal tissue of the same patient.

Animals

Male C57BL/6 mice (20−22 g) were purchased from Beijing Vital River Laboratory Animal Technology Co., Ltd. All mice were maintained in specific pathogen-free conditions, with an ambient temperature of 24 ± 2 °C, air humidity of 40−70%, and a 12 h dark/12 h light cycle. All animal procedures were performed under the guidelines approved by the Institutional Animal Care and Use Committee of Nanjing University (IACUC-2309002).

For the colitis model, mice were housed in groups of five mice per cage and acclimatized for 1 week before inclusion in the study. Mice received 2.5% (w/v) DSS supplemented in the sterilized drinking water for 7 days, followed by water. Healthy control mice received only water. Then, PBS, 200 μL of ECM solution, 10 mg/kg PB, and 10 mg/kg PB@ECM were administered *via* intravenous injection on day 6, day 8, and day 10. Changes in body weight were assessed daily over the 11-day experimental period, and samples were collected on day 12. On the last day of the experiment, mice were sacrificed, and the entire colon and other organs were excised. Colon length was measured and gently washed with physiological saline. Then, two pieces of the distal sections (0.5 cm in length) were used for H&E staining, alcian blue staining, immunohistochemistry (IL-6 and TNF-α), and immunofluorescence staining. Quantitative analysis of positively stained areas was conducted using ImageJ.

For the colitis-associated colon cancer model, mice were housed in groups of five mice per cage and acclimatized for 1 week before inclusion in the study. Mice were intraperitoneally (*i.p.*) injected with 10 mg/kg AOM 7 days prior to the first 2.5% DSS-induced colitis period. The early, intermediate, and late stages of colitis periods were induced by giving 2.5% DSS in drinking water for 7 days, followed by 14 days of regular drinking water. Healthy control mice received only water. Then, PBS, 200 μL of ECM solution, 10 mg/kg PB, and 10 mg/kg PB@ECM were administered *via* intravenous injection twice a week. Changes in body weight were assessed every couple of days over the experimental period. Mice were sacrificed, and the entire colon and other organs were excised at the end of each stage. Colon length was measured and gently washed with physiological saline. Then, the distal part of the 3 cm colon was made into Swiss roll. These Swiss rolls were used for H&E staining, alcian blue staining, immunohistochemistry (IL-6, TNF-α, and Ki67), and immunofluorescence staining. The survival curve of CAC mice was plotted to further evaluate the therapeutic effect of PB@ECM. Quantitative analysis of positively stained areas was conducted using ImageJ.

■ ASSOCIATED CONTENT

Supporting Information

The Supporting Information is available free of charge at https://pubs.acs.org/doi/10.1021/acsnano.6c16014.

Experimental procedures for nanozyme synthesis and characterization, enzyme-like activity assays, *in vitro* and *in vivo* evaluations, histological analysis, and transcriptomic analysis; additional data on physicochemical properties, cellular uptake, biodistribution, and biosafety evaluation; primer sequences, clinical information, and comparison statistics (Figures S1−S45 and Tables S1−S7) (PDF)

■ AUTHOR INFORMATION

Corresponding Authors

Hui Wei − *School of Chemistry, State Key Laboratory of Analytical Chemistry for Life Science, Chemistry and Biomedicine Innovation Center (ChemBIC), ChemBioMed Interdisciplinary Research Center at Nanjing University, Nanjing University, Nanjing, Jiangsu 210023, China; School of Biomedical Engineering, College of Engineering and Applied Sciences, Nanjing National Laboratory of Microstructures, Jiangsu Key Laboratory of Artificial Functional Materials, Nanjing University, Nanjing, Jiangsu 210023, China; Nanozyme Laboratory in Zhongyuan, Henan Academy of Innovations in Medical Science, Zhengzhou, Henan 451163, China;* orcid.org/0000-0003-0870-7142; Email: weihui@nju.edu.cn

Xiaoyu Wang − *Department of Chemistry and Material Science, College of Science, Nanjing Forestry University, Nanjing, Jiangsu 210037, China;* orcid.org/0000-0002-8641-2430; Email: wangxiaoyu@njfu.edu.cn

Xinying Wang − *Department of General Surgery, Jinling Hospital, Medical School of Nanjing University, Nanjing, Jiangsu 210002, China;* orcid.org/0000-0002-6611-9210; Email: wangxinying@nju.edu.cn

Jingjing Zhang − *School of Chemistry, State Key Laboratory of Analytical Chemistry for Life Science, Chemistry and Biomedicine Innovation Center (ChemBIC), ChemBioMed Interdisciplinary Research Center at Nanjing University, Nanjing University, Nanjing, Jiangsu 210023, China;* orcid.org/0000-0002-1041-793X; Email: jing15209791@nju.edu.cn

Authors

Qi Sun − *School of Chemistry, State Key Laboratory of Analytical Chemistry for Life Science, Chemistry and Biomedicine Innovation Center (ChemBIC), ChemBioMed Interdisciplinary Research Center at Nanjing University, Nanjing University, Nanjing, Jiangsu 210023, China; School of Biomedical Engineering, College of Engineering and Applied Sciences, Nanjing National Laboratory of Microstructures, Jiangsu Key Laboratory of Artificial Functional Materials, Nanjing University, Nanjing, Jiangsu 210023, China;* orcid.org/0009-0004-3613-2774

Wanling Liu − *School of Biomedical Engineering, College of Engineering and Applied Sciences, Nanjing National Laboratory of Microstructures, Jiangsu Key Laboratory of Artificial Functional Materials, Nanjing University, Nanjing, Jiangsu 210023, China*

Sijie Li − *Department of Chemistry and Material Science, College of Science, Nanjing Forestry University, Nanjing, Jiangsu 210037, China*

Xiwen Chen − *School of Biomedical Engineering, College of Engineering and Applied Sciences, Nanjing National Laboratory of Microstructures, Jiangsu Key Laboratory of Artificial Functional Materials, Nanjing University, Nanjing, Jiangsu 210023, China*

Hanjie Zhang − *School of Biomedical Engineering, College of Engineering and Applied Sciences, Nanjing National Laboratory of Microstructures, Jiangsu Key Laboratory of Artificial Functional Materials, Nanjing University, Nanjing, Jiangsu 210023, China;* orcid.org/0009-0006-7174-7736

Dongze Mo − *School of Biomedical Engineering, College of Engineering and Applied Sciences, Nanjing National Laboratory of Microstructures, Jiangsu Key Laboratory of Artificial Functional Materials, Nanjing University, Nanjing, Jiangsu 210023, China*

Pinwen Zhou − *Department of General Surgery, Jinling Hospital, Medical School of Nanjing University, Nanjing, Jiangsu 210002, China;* orcid.org/0000-0003-1268-2806

Xiaomiao Cui − *School of Biomedical Engineering, College of Engineering and Applied Sciences, Nanjing National*

Downloaded from pubs.acs.org/ancac3/article-pdf/doi/10.1021/acsnano.6c16014/6914824O/acsnano.6c16014.pdf?guestAccessKey=8de0abfb-c7d9-4588-addc-2b5c448d3cea by NANJING UNIV user on 12 November 2026

Laboratory of Microstructures, Jiangsu Key Laboratory of Artificial Functional Materials, Nanjing University, Nanjing, Jiangsu 210023, China; orcid.org/0000-0002-5594-9390

Di Huang − *Department of Chemistry and Material Science, College of Science, Nanjing Forestry University, Nanjing, Jiangsu 210037, China*

Bing Xia − *Department of Chemistry and Material Science, College of Science, Nanjing Forestry University, Nanjing, Jiangsu 210037, China;* orcid.org/0000-0002-1637-7908

Complete contact information is available at: https://pubs.acs.org/10.1021/acsnano.6c16014

Notes

The authors declare no competing financial interest.

■ ACKNOWLEDGMENTS

We thank Mr. Jiang Du for help in BET testing and Dr. Gen Wei for help in EPR testing. We thank BioRender for the illustration tools. Created in BioRender. Qi, S. (2026) https://BioRender.com/l25c561. This work was supported by the National Natural Science Foundation of China (W2512074 and 22374071), the Key Program of Nanozyme Laboratory in Zhongyuan (NLZ-KP2024NIC06), the Natural Science Foundation of Jiangsu Province (BK20241895), the Jiangsu Provincial Key R&D Program (BE2022836), the State Key Laboratory of Analytical Chemistry for Life Science (5431ZZXM2501), the Fundamental Research Funds for the Central Universities (2025300292), the PAPD Program, and the International Expansion and Enhancement Program by Nanjing University International Affairs Office.

■ REFERENCES

(1) Furman, D.; Campisi, J.; Verdin, E.; Carrera-Bastos, P.; Targ, S.; Franceschi, C.; Ferrucci, L.; Gilroy, D. W.; Fasano, A.; Miller, G. W.; Miller, A. H.; Mantovani, A.; Weyand, C. M.; Barzilai, N.; Goronzy, J. J.; Rando, T. A.; Effros, R. B.; Lucia, A.; Kleinstreuer, N.; Slavich, G. M. Chronic inflammation in the etiology of disease across the life span. *Nat. Med.* **2019**, *25*, 1822−1832.

(2) Xie, Y.; Liu, F.; Wu, Y.; Zhu, Y.; Jiang, Y.; Wu, Q.; Dong, Z.; Liu, K. Inflammation in cancer: therapeutic opportunities from new insights. *Mol. Cancer* **2025**, *24* (1), 51.

(3) Coussens, L. M.; Zitvogel, L.; Palucka, A. K. Neutralizing Tumor-Promoting Chronic Inflammation: A Magic Bullet? *Science* **2013**, *339*, 286−291.

(4) Crusz, S. M.; Balkwill, F. R. Inflammation and cancer: advances and new agents. *Nat. Rev. Clin. Oncol.* **2015**, *12*, 584−596.

(5) Zhao, H.; Wu, L.; Yan, G.; Chen, Y.; Zhou, M.; Wu, Y.; Li, Y. Inflammation and tumor progression: signaling pathways and targeted intervention. *Signal Transduct. Target. Ther.* **2021**, *6* (1), 263.

(6) Grivennikov, S. I.; Greten, F. R.; Karin, M. Immunity, inflammation, and cancer. *Cell* **2010**, *140*, 883−899.

(7) Fajgenbaum, D. C.; June, C. H. Cytokine Storm. *N. Engl. J. Med.* **2020**, *383*, 2255−2273.

(8) Greten, F. R.; Grivennikov, S. I. Inflammation and cancer: triggers, mechanisms, and consequences. *Immunity* **2019**, *51*, 27−41.

(9) Fournier, B. M.; Parkos, C. A. The role of neutrophils during intestinal inflammation. *Mucosal Immunol.* **2012**, *5*, 354−366.

(10) Verhagen, M. P.; Schmitt, M.; Fodde, R. Western lifestyle, metaflammation and the cell of origin of colon cancer. *Nat. Rev. Gastroenterol. Hepatol.* **2024**, *21*, 603−604.

(11) Terzić, J.; Grivennikov, S.; Karin, E.; Karin, M. Inflammation and colon cancer. *Gastroenterology* **2010**, *138*, 2101−2114.

(12) Kobayashi, T.; Siegmund, B.; Le Berre, C.; Wei, S. C.; Ferrante, M.; Shen, B.; Bernstein, C. N.; Danese, S.; Peyrin-Biroulet, L.; et al. Ulcerative colitis. *Nat. Rev. Methods Primers* **2020**, *6* (1), 74.

(13) Roda, G.; Chien Ng, S.; Kotze, P. G.; Argollo, M.; Panaccione, R.; Spinelli, A.; Kaser, A.; Peyrin-Biroulet, L.; Danese, S. Crohn's disease. *Nat. Rev. Methods Primers* **2020**, *6* (1), 22.

(14) Eaden, J. A.; Abrams, K. R.; Mayberry, J. F. The risk of colorectal cancer in ulcerative colitis: a meta-analysis. *Gut* **2001**, *48*, 526−535.

(15) Shah, S. C.; Itzkowitz, S. H. Colorectal Cancer in Inflammatory Bowel Disease: Mechanisms and Management. *Gastroenterology* **2022**, *162*, 715−730.

(16) Nagarsheth, N.; Wicha, M. S.; Zou, W. Chemokines in the cancer microenvironment and their relevance in cancer immunotherapy. *Nat. Rev. Immunol.* **2017**, *17*, 559−572.

(17) Yi, M.; Li, T.; Niu, M.; Zhang, H.; Wu, Y.; Wu, K.; Dai, Z. Targeting cytokine and chemokine signaling pathways for cancer therapy. *Signal Transduct. Target. Ther.* **2024**, *9* (1), 176.

(18) Tecchio, C.; Cassatella, M. A. Neutrophil-derived chemokines on the road to immunity. *Semin. Immunol.* **2016**, *28*, 119−128.

(19) Adrover, J. M.; Del Fresno, C.; Crainiciuc, G.; Cuartero, M. I.; Casanova-Acebes, M.; Weiss, L. A.; Huerga-Encabo, H.; Silvestre-Roig, C.; Rossaint, J.; Cossío, I.; Lechuga-Vieco, A. V.; García-Prieto, J.; Gómez-Parrizas, M.; Quintana, J. A.; Ballesteros, I.; Martin-Salamanca, S.; Aroca-Crevillen, A.; Chong, S. Z.; Evrard, M.; Balabanian, K.; López, J.; Bidzhekov, K.; Bachelerie, F.; Abad-Santos, F.; Muñoz-Calleja, C.; Zarbock, A.; Soehnlein, O.; Weber, C.; Ng, L. G.; Lopez-Rodriguez, C.; Sancho, D.; Moro, M. A.; Ibáñez, B.; Hidalgo, A. A neutrophil timer coordinates immune defense and vascular protection. *Immunity* **2019**, *50*, 390−402.

(20) Zhang, W.; Hu, S.; Yin, J.; He, W.; Lu, W.; Ma, M.; Gu, N.; Zhang, Y. Prussian blue nanoparticles as multienzyme mimetics and reactive oxygen species scavengers. *J. Am. Chem. Soc.* **2016**, *138*, 5860−5865.

(21) Gao, W.; Wang, Y.; Zheng, Y.; Cai, X. Prussian Blue Nanoparticle: From a Photothermal Conversion Agent and a Drug Delivery System, to a Bioactive Drug. *Acc. Mater. Res.* **2024**, *5*, 687−698.

(22) Li, C.; Tang, Z.; Zhang, W.; Ye, Z.; Liu, F. GEPIA2021: integrating multiple deconvolution-based analysis into GEPIA. *Nucleic Acids Res.* **2021**, *49*, W242−W246.

(23) Ru, B.; Wong, C. N.; Tong, Y.; Zhong, J. Y.; Zhong, S. S. W.; Wu, W. C.; Chu, K. C.; Wong, C. Y.; Lau, C. Y.; Chen, I.; et al. TISIDB: an integrated repository portal for tumor-immune system interactions. *Bioinformatics* **2019**, *35* (20), 4200−4202.

(24) Acharyya, S.; Oskarsson, T.; Vanharanta, S.; Malladi, S.; Kim, J.; Morris, P. G.; Manova-Todorova, K.; Leversha, M.; Hogg, N.; Seshan, V. E.; Norton, L.; Brogi, E.; Massagué, J. A CXCL1 paracrine network links cancer chemoresistance and metastasis. *Cell* **2012**, *150*, 165−178.

(25) Deng, H.; Kan, A.; Lyu, N.; He, M.; Huang, X.; Qiao, S.; Li, S.; Lu, W.; Xie, Q.; Chen, H.; Lai, J.; Chen, Q.; Jiang, X.; Liu, S.; Zhang, Z.; Zhao, M. Tumor-derived lactate inhibit the efficacy of lenvatinib through regulating PD-L1 expression on neutrophil in hepatocellular carcinoma. *J. Immunother Cancer* **2021**, *9*, No. e002305.

(26) La'ah, A. S.; Tsai, P. H.; Yarmishyn, A. A.; Ching, L. J.; Chen, C. Y.; Chien, Y.; Chen, J. C.-Y.; Tsai, M. L.; Chen, Y. C.; Ma, C.; et al. Neutrophils Recruited by NKX2-1 Suppression via Activation of CXCLs/CXCR2 Axis Promote Lung Adenocarcinoma Progression. *Adv. Sci.* **2024**, *11* (38), 2400370.

(27) De Filippo, K.; Dudeck, A.; Hasenberg, M.; Nye, E.; van Rooijen, N.; Hartmann, K.; Gunzer, M.; Roers, A.; Hogg, N. Mast cell and macrophage chemokines CXCL1/CXCL2 control the early stage of neutrophil recruitment during tissue inflammation. *Blood* **2013**, *121*, 4930−4937.

(28) Liu, S.; Liu, J.; Yang, X.; Jiang, M.; Wang, Q.; Zhang, L.; Ma, Y.; Shen, Z.; Tian, Z.; Cao, X.; et al. *Cis*-acting lnc-*Cxcl2* restrains neutrophil-mediated lung inflammation by inhibiting epithelial cell CXCL2 expression in virus infection. *Proc. Natl. Acad. Sci. U. S. A.* **2021**, *118*, No. e2108276118.

(29) Li, J.; Liu, X.; Tan, L.; Cui, Z.; Yang, X.; Liang, Y.; Li, Z.; Zhu, S.; Zheng, Y.; Yeung, K. W. K.; et al. Zinc-doped Prussian blue enhances photothermal clearance of Staphylococcus aureus and promotes tissue repair in infected wounds. *Nat. Commun.* **2019**, *10* (1), 4490.

Downloaded from pubs.acs.org/ancac3/article-pdf/doi/10.1021/acsnano.6c16014/6914824/acsnano.6c16014.pdf?guestAccessKey=8de0abfb-c7d9-4588-addc-2b5c448d3cea by NANJING UNIV user on 12 November 2026

(30) Deng, R.; Zhao, R.; Zhang, Z.; Chen, Y.; Yang, M.; Lin, Y.; Ye, J.; Li, N.; Qin, H.; Yan, X.; et al. Chondrocyte membrane−coated nanoparticles promote drug retention and halt cartilage damage in rat and canine osteoarthritis. *Sci. Transl. Med.* **2024**, *16* (735), No. eadh9751.
(31) Li, S.; Men, Y.; Wang, Z.; Wu, Y.; Sun, H.; Yin, M.; Fan, X.; Deng, G.; Yang, Z.; Yang, T.; Xiao, Y.; Zhou, H.; Wang, G.; Fan, J.; Xu, C.; Gao, Q.; Han, S. Amplifying antigen-induced cellular responses with proximity labelling. *Nature* **2025**, *647*, 506−516.
(32) Zhang, R.; Yan, X.; Gao, L.; Fan, K. Nanozymes expanding the boundaries of biocatalysis. *Nat. Commun.* **2025**, *16*, 6817.
(33) Li, J.; Huang, J.; Lyu, Y.; Huang, J.; Jiang, Y.; Xie, C.; Pu, K. Photoactivatable Organic Semiconducting Pro-nanoenzymes. *J. Am. Chem. Soc.* **2019**, *141*, 4073−4079.
(34) Zhang, Y.; Wei, G.; Liu, W.; Li, T.; Wang, Y.; Zhou, M.; Liu, Y.; Wang, X.; Wei, H. Nanozymes for nanohealthcare. *Nat. Rev. Methods Primers* **2024**, *4*, 36.
(35) Cao, F.; Jin, L.; Gao, Y.; Ding, Y.; Wen, H.; Qian, Z.; Zhang, C.; Hong, L.; Yang, H.; Zhang, J.; Tong, Z.; Wang, W.; Chen, X.; Mao, Z. Artificial-enzymes-armed *Bifidobacterium longum* probiotics for alleviating intestinal inflammation and microbiota dysbiosis. *Nat. Nanotechnol.* **2023**, *18*, 617−627.
(36) Zhao, S.; Li, Y.; Liu, Q.; Li, S.; Cheng, Y.; Cheng, C.; Sun, Z.; Du, Y.; Butch, C. J.; Wei, H. An orally administered CeO_2@montmorillonite nanozyme targets inflammation for inflammatory bowel disease therapy. *Adv. Funct. Mater.* **2020**, *30* (45), 2004692.
(37) Chen, Z.; Zhu, Y.; You, Y.; Ge, M.; Chen, Y.; Lin, H.; Shi, J. Enzyme-Mimic Activities of RuCo Bimetallic Nanosheets for Inflammatory Bowel Disease Treatment. *J. Am. Chem. Soc.* **2025**, *147*, 13424−13436.
(38) Liu, W.; Zhang, Y.; Wei, G.; Zhang, M.; Li, T.; Liu, Q.; Zhou, Z.; Du, Y.; Wei, H. Integrated cascade nanozymes with antisenescence activities for atherosclerosis therapy. *Angew. Chem., Int. Ed.* **2023**, *62*, No. e202304465.
(39) He, Z.; Chen, W.; Hu, K.; Luo, Y.; Zeng, W.; He, X.; Li, T.; Ouyang, J.; Li, Y.; Xie, L.; Zhang, Y.; Xu, Q.; Yang, S.; Guo, M.; Zou, W.; Li, Y.; Huang, L.; Chen, L.; Zhang, X.; Saiding, Q.; Wang, R.; Zhang, M.; Kong, N.; Xie, T.; Song, X.; Tao, W. Resolvin D1 delivery to lesional macrophages using antioxidative black phosphorus nanosheets for atherosclerosis treatment. *Nat. Nanotechnol.* **2024**, *19*, 1386−1398.
(40) Feng, K.; Sun, L.; Zhou, Z.; Zhang, J. A.; Fang, R. H.; Gao, W.; Zhang, L. Macrophage-mimicking nanodiscs for treating systemic infection caused by methicillin-resistant *Staphylococcus aureus*. *Sci. Adv.* **2025**, *11*, No. eadw7511.
(41) Liu, L.; Pan, D.; Chen, S.; Martikainen, M. V.; Kårlund, A.; Ke, J.; Pulkkinen, H.; Ruhanen, H.; Roponen, M.; Käkelä, R.; et al. Systematic design of cell membrane coating to improve tumor targeting of nanoparticles. *Nat. Commun.* **2022**, *13*, 6181.
(42) Han, T.; Zhu, W.; Xu, R.; Chiang, S. T.; Jin, X.; Shen, X.; Qian, C.; Yang, G.; Li, R.; Ai, X. Glycan-Modified Cellular Nanosponges for Enhanced Treatment of Cholera Toxin-Induced Secretory Diarrhea. *J. Am. Chem. Soc.* **2025**, *147*, 16982−16991.
(43) Sun, L.; Yu, Y.; Zhang, J. A.; Shen, W.; Feng, K.; Bai, D.; Zhou, Z.; Gao, W.; Zhang, L. Controlled Dimerization of Cellular Nanodiscs via Click Chemistry to Enhance Immune Compatibility. *J. Am. Chem. Soc.* **2025**, *147*, 30136−30145.

Downloaded from pubs.acs.org/ancac3/article-pdf/doi/10.1021/acsnano.6c16014/6914824O/acsnano.6c16014.pdf?guestAccessKey=8de0abfb-c7d9-4588-addc-2b5c448d3cea by NANJING UNIV user on 12 November 2026

https://doi.org/10.1021/acsnano.6c16014
ACS Nano XXXX, XXX, XXX−XXX